

LLRF Controls and Feedback: Free-Electron Lasers and Energy Recovery Linacs

S. Pfeiffer

DESY, Hamburg, Germany

Abstract

The low-level radio frequency (LLRF) system generates the drive sent to the high-power components. In this paper, we give the basics of LLRF controls and feedback. This includes a brief introduction to the two concepts for this school, i.e., the energy recovery linac and the free-electron laser, and their main differences, from a LLRF perspective. The physical behaviour of the subcomponents (detector, amplifier, cavity, etc.) within an LLRF feedback loop is outlined, together with its system modelling in the time and frequency domains. System identification using special input–output signals is introduced. Furthermore, stability checks for the closed-loop operation and the feedback controller design in the time and frequency domains are briefly discussed. This paper concludes with some examples for system identification, its feedback design, and the achieved stability at different facilities, showing the need for LLRF control and feedback operation.

Keywords

Low-level radio frequency; LLRF; feedback; system identification; controller design.

1 Introduction

Low-level RF (LLRF) field control is used to stabilize the accelerating field inside normal- and superconducting RF cavities, mainly using digital feedback loops. Optimal feedback regulation is part of this contribution and discussed in this paper. First, a brief introduction to energy recovery linacs and free-electron lasers is given. Here, the main focus is on the differences between both concepts. At the end of this section, a short introduction to the need for LLRF controls is discussed. The mathematical modelling of certain components within the feedback loop (Section 2) is often necessary to optimize the feedback controller. An alternative to this mathematical modelling using differential equations is system identification using special excitation signals and relating them to the corresponding output signal (Section 3). Based on such a system model, the optimal feedback controller can be designed in the time or frequency domain, as shown in Section 4. Examples for the system identification and the feedback controller design are discussed in Section 5, justifying the need of LLRF controls and feedback.

1.1 Energy recovery linac

An energy recovery linac concept is given in the CAS 2016 contribution from Dr. A. Jankowiak (HZB) *Concept of ERL*. At bERLinPro, the beam current will be 100 mA and the accelerating structures are superconducting RF cavities operated in continuous wave mode at an RF frequency of 1.3 GHz [1–3]. Another energy recovery linac, the compact energy recovery linac at KEK, is described in the following [4]. The compact energy recovery linac is an ongoing project at KEK, intended to demonstrate excellent energy recovery linac performance towards a future light source. The compact energy recovery linac is illustrated in Fig. 1. The injector consists of a photocathode d.c. gun, a normal-conducting buncher cavity with a loaded quality factor (Q_L) of 1.1×10^5 and three two-cell superconducting cavities operated with $Q_L = 5 \times 10^5$. The recirculation loop hosts several magnets (dipoles and quadrupoles), the

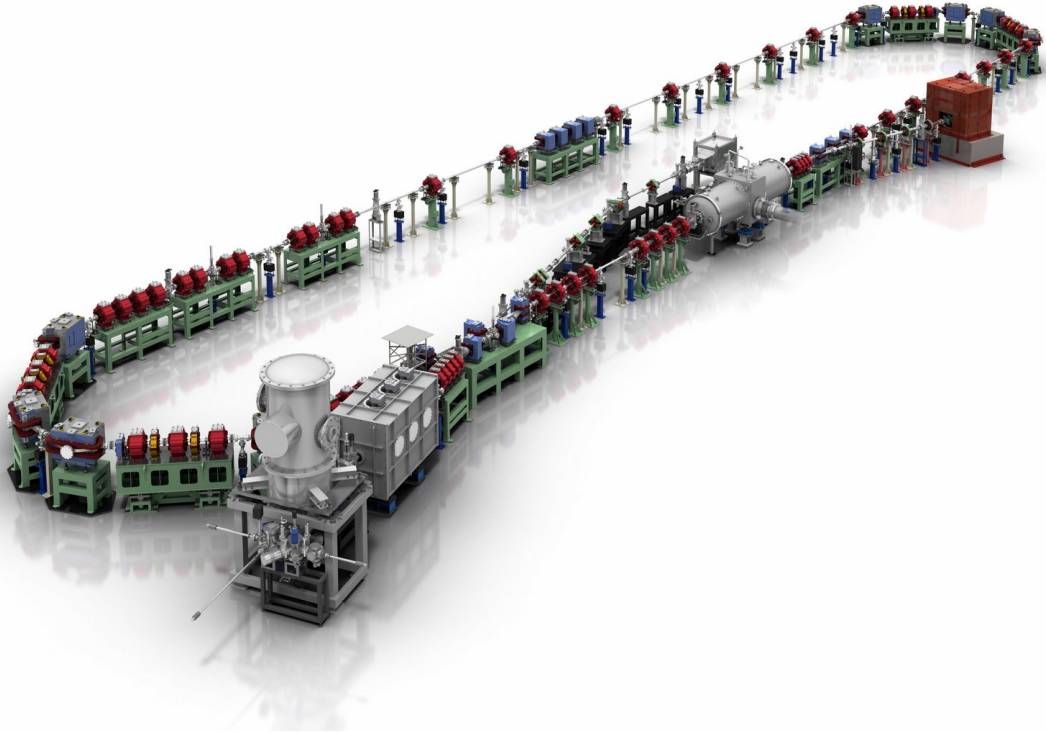


Fig. 1: Compact energy recovery linac ©Rey.Hori/KEK [6]: the injector part (located in the lower left) and the recirculation loop are shown.

Table 1: Example RF and beam parameters for energy recovery linac and free-electron laser

	Compact energy recovery linac	bERLinPro	FLASH
Desired RF stability (r.m.s.)	$\Delta A/A \leq 0.1\%$ $\Delta\varphi \leq 0.1^\circ$	$\Delta A/A \leq 0.05\%$ $\Delta\varphi \leq 0.02^\circ-0.1^\circ$	$\Delta A/A \leq 0.01\%$ $\Delta\varphi \leq 0.01^\circ$
Loaded quality factor Q_L	$1.1 \times 10^5-1 \times 10^7$	$1 \times 10^5-5 \times 10^7$	$1.2 \times 10^5-3 \times 10^6$
Nominal beam energy	35 MeV	50 MeV	max. 1.25 GeV
Beam current	~ 100 mA	~ 100 mA	~ 1 mA
Mode of operation	Continuous wave	Continuous wave	Pulsed

beam diagnostics (e.g., beam position monitors), and two nine-cell superconducting cavities operated with $Q_L = 1 \times 10^7$. The RF frequency for all cavities is 1.3 GHz. For the compact energy recovery linac, a RF field stability of 0.1% in amplitude and 0.1° in phase is required [5]. The compact energy recovery linac is operated in continuous wave mode with a beam current of up to 100 mA; normal- and superconducting RF structures, powered with klystrons and solid state amplifiers, are used to accelerate the beam to its target energy.

Energy recovery linacs are widely used in research facilities. The beam current is of the order of 100 mA; it is foreseen to increase to the ampere regime. Normal- and superconducting RF cavities are used to reach the final target energy. The cavities are driven by klystrons, solid state amplifiers, or inductive output tubes. The key parameters of this compact energy recovery linac at KEK and the bERLinPro at HZB are given in Table 1.

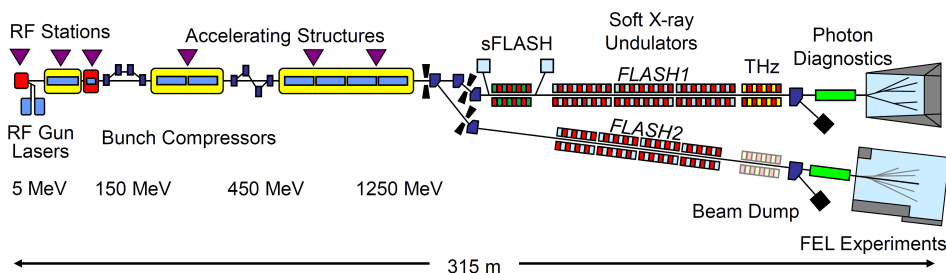


Fig. 2: FLASH: beam direction is from left to right. Both beamlines are shown, the old FLASH1 beamline and the new FLASH2 beamline [7].

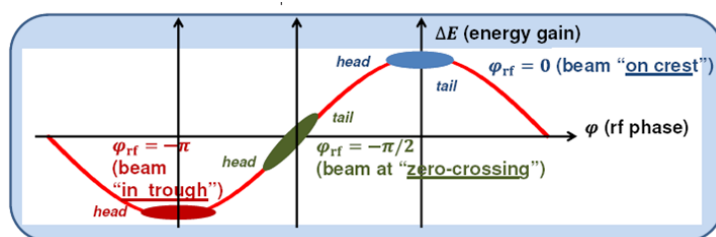


Fig. 3: Location of electron bunch for different phase settings [8]

1.2 Free-electron laser

The free-electron laser (FLASH) is the world's first soft X-ray free-electron laser (XFEL). It is a linear accelerator with a total length of about 315 m [7]. Electron bunches are generated using an external laser and a photocathode inside the normal-conducting RF-gun ($Q_L \approx 1.2 \times 10^5$). They are further accelerated by 56 superconducting RF cavities operated at 1.3 GHz with $Q_L = 3 \times 10^6$ in seven cryomodules. Each cryomodule is depicted in Fig. 2 as a blue box hosting eight superconducting RF cavities. Furthermore, four superconducting RF cavities (red box with one cryomodule) operated at 3.9 GHz, i.e., the third harmonic of 1.3 GHz, are used for phase space linearization. The cavities at FLASH are all driven by klystrons. Up to a maximum of 16 cavities are driven by one klystron, for cost efficiency. FLASH is operated in short-pulse mode with a repetition rate of 10 Hz and 800 μ s maximum beam time. Each RF pulse is active for about 1.4 ms (including fill time and beam time), corresponding to a duty factor of about 1%. During the beam time a maximum of 800 electron bunches at 1 MHz repetition rate can be used for experiments. The maximum final bunch energy is 1.25 GeV, corresponding to a fundamental laser light wavelength of 4.12 nm using fixed gap undulators at the FLASH1 beamline. The maximum bunch charge of each electron bunch is of the order of 1 nC; therefore, the maximum beam current is of the order of 1 mA (1 nC bunch at 1 MHz repetition rate), instead of 100 mA for an energy recovery linac, see Table 1.

1.3 LLRF in general—control goal

The LLRF system is used to supply the accelerating cavities with high-power RF signals. Furthermore, it is used to modify or adjust the accelerating field in amplitude and phase (A/P). The desired A/P value depends on the mode of operation, i.e., acceleration, deceleration, or an imposed energy chirp, see Fig. 3. The typical RF stability of an accelerating section is of the order of $\Delta A/A \leq 0.1\% - 0.01\%$ and $\Delta\varphi \leq 0.1^\circ - 0.01^\circ$.

Consider, e.g., a free-electron laser with a bunch compressor to achieve high peak currents. Its injector laser stability, cavity amplitude, phase stability are directly related to the timing jitter after a bunch compressor defining the achievable free-electron laser performance, see contribution from Dr. M. Divall (PSI) *Lasers in FEL Facilities*. This requires a precise timing and synchronization of the master

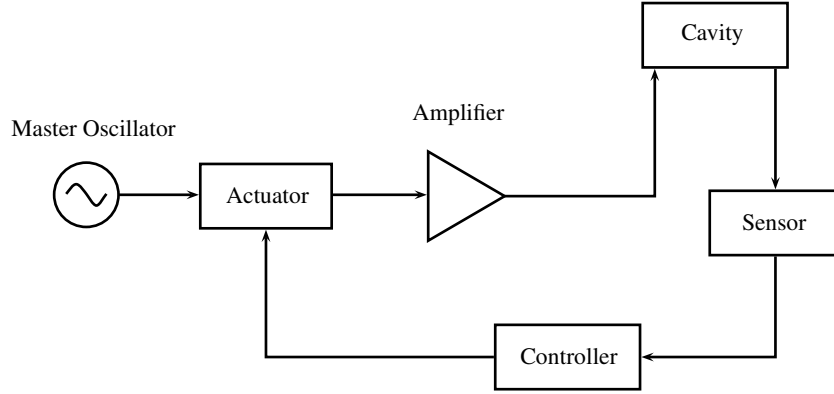


Fig. 4: The LLRF control loop with master oscillator, actuator, amplifier, cavity, and sensor. The controller closes the feedback loop.

clock and all attached subdevices, such as the accelerating modules. For now, we will assume that the timing and synchronization are perfect.

We will start with the description of the closed-loop system to be controlled. An example of a LLRF feedback control loop is depicted in Fig. 4. The master oscillator provides a constant sinusoidal signal with the desired frequency, e.g., 1.3 GHz. This master oscillator signal is amplified from low power (a few volts) to high power to drive the cavity. A sensor, e.g., a pick-up or magnetic loop, is placed inside the cavity to detect a fraction of the RF field. This information is used by a controller to control the amplitude and phase inside the cavity by modulating the amplitude and phase of the master oscillator signal. This closes the feedback loop. The LLRF regulates on a low power signal, while only the part after the amplifier and in the cavity are operated at high power (e.g., in the megavolt regime).

In the following we will discuss the individual blocks separately before modelling the system behaviour to optimize the controller.

2 System description

In this section, we will focus on the individual blocks within a feedback loop for the LLRF system. A brief overview is given in Fig. 4.

2.1 RF detection

The principles of RF field detection are based on mixing a reference signal (LO) with the RF signal to be detected. Here, the goal is to measure the amplitude and phase, or the in-phase (I) and quadrature (Q) part of an RF signal with respect to a reference signal. The relation between A/P and I/Q is:

$$\begin{aligned} I &= A \cdot \cos \varphi & A &= \sqrt{I^2 + Q^2} \\ Q &= A \cdot \sin \varphi & \varphi &= \text{atan2}(Q, I), \end{aligned}$$

with

$$\text{atan2}(Q, I) = \begin{cases} \arctan\left(\frac{Q}{I}\right) & \text{if } I > 0, \\ \arctan\left(\frac{Q}{I}\right) + \pi & \text{if } I < 0 \text{ and } Q \geq 0, \\ \arctan\left(\frac{Q}{I}\right) - \pi & \text{if } I < 0 \text{ and } Q < 0, \\ +\frac{\pi}{2} & \text{if } I = 0 \text{ and } Q > 0, \\ -\frac{\pi}{2} & \text{if } I = 0 \text{ and } Q < 0, \\ \text{undefined} & \text{if } I = 0 \text{ and } Q = 0. \end{cases}$$

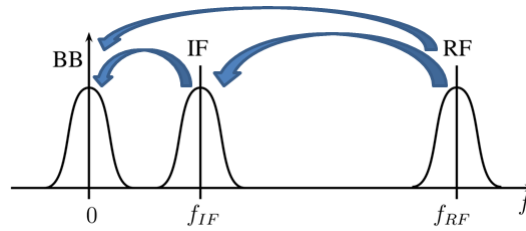


Fig. 5: RF down-sampling directly to baseband (BB) or via an intermediate frequency (IF)

The high-frequency signal is down-converted to the baseband. Different amplitude and phase conditions between the RF and the LO are responsible for the corresponding output signal (A/P or I/Q). Only a short overview of different detection schemes is given; detailed information can be found in Ref. [9].

The briefly discussed detection schemes are:

1. direct amplitude and phase detection:
 - no down-conversion;
 - analogue or digital (up to 800 MHz analogue-to-digital converters);
2. baseband sampling (analogue I/Q detector);
3. digital I/Q sampling;
4. intermediate-frequency sampling (non-I/Q sampling).

Scheme (1) is a direct sampling scheme, while schemes (2)–(4) are based on mixing a reference signal (LO) with the RF signal, meaning that the RF signal is down-converted into baseband directly or using an intermediate frequency, see Fig. 5.

2.1.1 Analogue direct amplitude and phase detection

The analogue amplitude and phase detection are achieved by splitting the RF signal into two parts, see Fig. 6. The first part is used to detect the amplitude using a diode. The second part is mixed with a frequency- and phase-stable LO signal (the same frequency as the expected RF signal), leading, for small angle variations, to a signal proportional to the phase difference between the RF and LO signal. The mathematical description for the phase signal is given by:

Input signals:

$$V_{\text{RF}}(t) = A_{\text{RF}} \sin(\omega t + \varphi_0),$$

$$V_{\text{LO}}(t) = A_{\text{LO}} \cos(\omega t),$$

Output signal:

$$V_{\text{mixer}} = A_{\text{RF}} \sin(\omega t + \varphi_0) \cdot A_{\text{LO}} \cos(\omega t) = \frac{A_{\text{RF}} A_{\text{LO}}}{2} (\sin(\varphi_0) + \sin(2\omega t + \varphi_0)),$$

Output signal after low-pass filtering:

$$V_{\text{LPF}} = \frac{A_{\text{RF}} A_{\text{LO}}}{2} \sin(\varphi_0) \approx \frac{A_{\text{RF}} A_{\text{LO}}}{2} \varphi_0 \quad (\text{for small } \varphi_0).$$

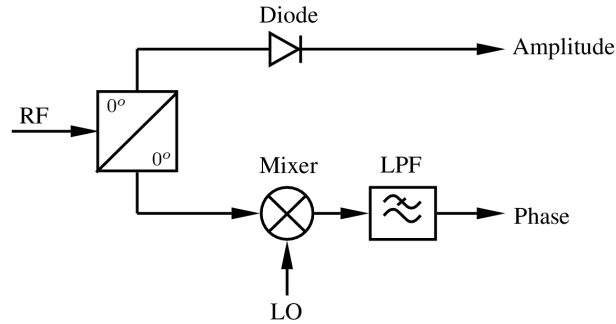


Fig. 6: Basic principle of analogue direct amplitude and phase detection

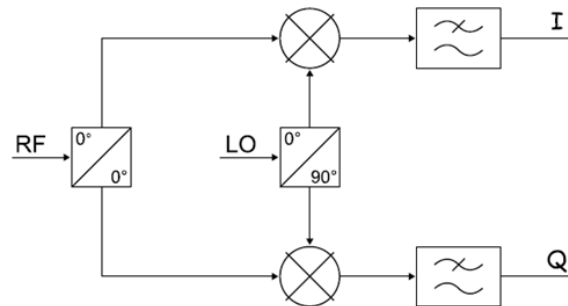


Fig. 7: Analogue I/Q detection [9]

2.1.2 Digital direct amplitude and phase detection

Nowadays, high-speed analogue-to-digital converters are available with sampling rates of more than 500 megasamples per second and analogue input bandwidth of up to 1.5 GHz. These analogue-to-digital converters enable the RF signal to be sampled directly without any RF converter or intermediate-frequency scheme, with a signal-to-noise ratio of more than 50 dB. The advantage is the reduction of the number of input stages for pre-configuration (down-conversion, filter, amplifier, etc.), reducing possible errors and noise sources and increasing reliability. The disadvantage is the increasing impact of the clock jitter on the signal-to-noise ratio for higher input frequencies. This effect is linear and can be reduced by the process gain due to digital band-limitation and averaging as a function of the square root. If digital filtering is used to filter out noise components outside the bandwidth, then the process gain must be included in the equation to account for the resulting increase in the signal-to-noise ratio using an N -bit analogue-to-digital converter, as shown in Eq. (1):

$$\text{signal-to-noise ratio} = 6.02 \times N + 1.76 \text{ dB} + 10 \log_{10} \frac{f_s}{2 \times f_{\text{BW}}} . \quad (1)$$

See, in addition, Ref. [10] for the noise characteristics and measurements performed at FLASH.

2.1.3 Baseband sampling (analogue I/Q detector)

This concept is an analogue I/Q detector, in which a direct conversion from RF to baseband is performed. The RF signal is multiplied by the LO signal resulting in analogue I/Q signals. Here, the LO signal is split by a hybrid and one signal is given a phase difference of 90° , see Fig. 7. Two analogue-to-digital converters are required for the digitization of an I/Q pair; hence, it requires more space and leads to higher cost than using only one analogue-to-digital converter, and the reliability is reduced. The main problem of this scheme is the phase-dependent amplitude detection due to I/Q imbalances and offsets, see Fig. 8.

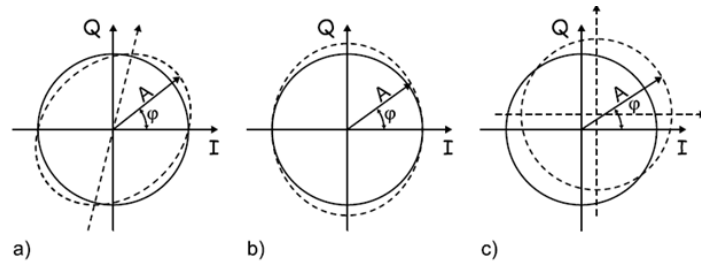


Fig. 8: Constellation diagram with different errors in I and Q . (a) The output signals of the mixers are not exactly I and Q , i.e., the phase difference is not 90° . (b) Gain mismatch between I and Q mixer branch. (c) I/Q offset at the mixer outputs [9].

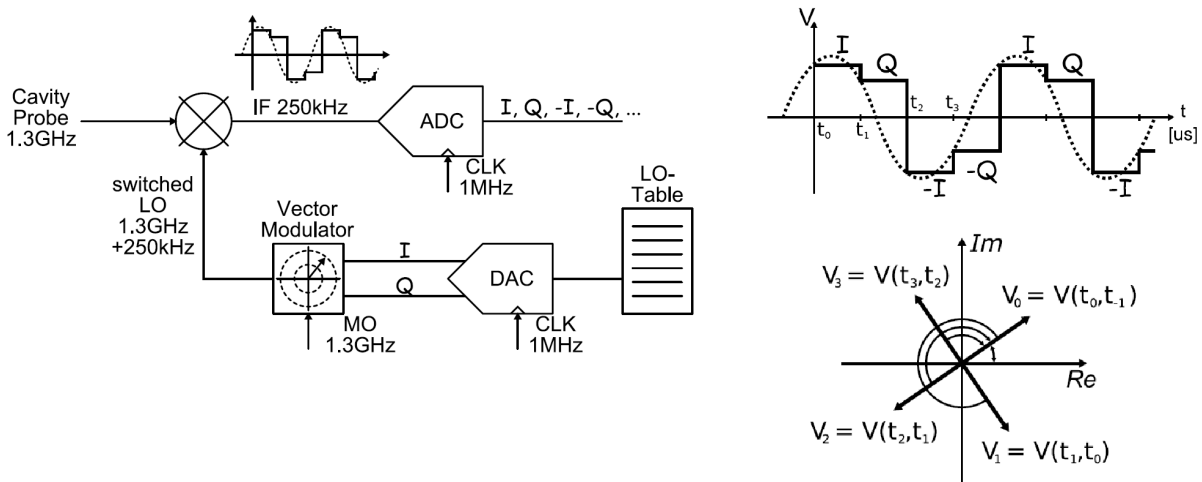


Fig. 9: Left-hand side: digital I/Q sampling scheme. Right-hand side: corresponding output sequence in time and complex domains [9].

2.1.4 Digital I/Q sampling

This detection scheme is similar to baseband sampling, but here only one analogue-to-digital converter and a switched LO are required, see Fig. 9. The LO signal after each sampling is switched in phase by 90° for a fixed time interval, leading to an output signal that represents a series of $I, Q, -I, -Q, \dots$ and so on. If the signal to be detected is of low bandwidth, or if it can be assumed that the signal does not change significantly between two samples, the field vector can be computed by two consecutive samples (I/Q value). To do this, the signal needs to be shifted by $n \times 90^\circ$ ($n = 0, 1, 2, 3$). The problem for this scheme is that the Nyquist frequency is $f_s/4$. Furthermore, owing to the switching with rectangular output signal, the entire signal chain needs a relatively high bandwidth.

2.1.5 Intermediate-frequency sampling (non- I/Q sampling)

In contrast with the conversion directly from RF to baseband, the RF can be first mixed down to an intermediate frequency and sampled. The detection scheme is depicted in Fig. 10. Based on the sampled analogue-to-digital converter signals, the actual I/Q detection is achieved by multiplication of the input signal by a sine and a cosine function on a digital level. The advantage of this scheme is that, e.g., phase and gain imbalance of the two multipliers of an analogue IQ -detector do not exist. For a series of samples, the series of $I[i]$ and $Q[i]$ are calculated by:

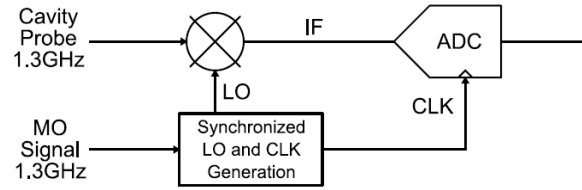


Fig. 10: Intermediate-frequency (IF) sampling principle with LO and clock (CLK) generation synchronized to the master oscillator (MO) [9]

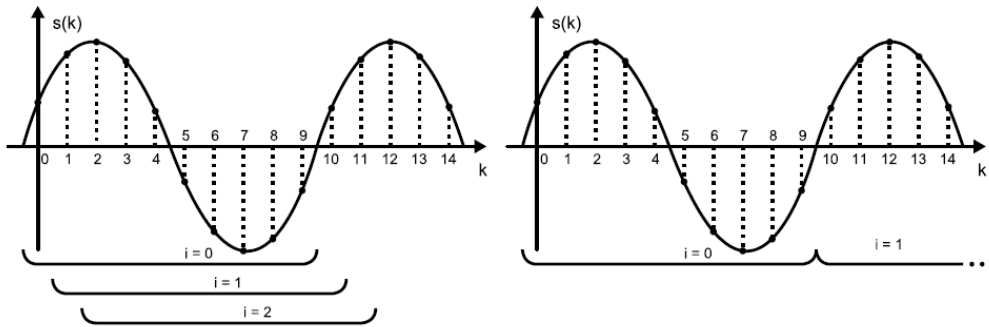


Fig. 11: Intermediate-frequency sampling: left-hand side, with sliding window detection; right-hand side, with step window detection [9]

(1) sliding window detection (left-hand plot in Fig. 11):

$$I(i) = \frac{2}{M} \sum_{k=0}^{M-1} s(k+i) \cos((k+i)\Delta\varphi),$$

$$Q(i) = \frac{2}{M} \sum_{k=0}^{M-1} s(k+i) \sin((k+i)\Delta\varphi);$$

(2) step window detection (right plot in Fig. 11):

$$I(i) = \frac{2}{M} \sum_{k=0}^{M-1} s(k+iM) \cos((k+iM)\Delta\varphi),$$

$$Q(i) = \frac{2}{M} \sum_{k=0}^{M-1} s(k+iM) \sin((k+iM)\Delta\varphi).$$

For further details, see, e.g., Ref. [9].

2.2 RF manipulation using a vector modulator

A vector modulator is often used to up-convert a baseband signal in I/Q coordinates back to an RF signal. The basic operation of a vector modulator is shown in Fig. 12. The signal from the master oscillator $y_{in}(t)$ is split into two parts, i.e., a 0° and a 90° part. The baseband I/Q values are multiplied with the corresponding sine and cosine parts. The sum of both signals leads to the RF output signal, i.e., the signal to the klystron, which is modulated by the I/Q components. In this way, the amplitude and phase of the RF output signal can be modulated by an I/Q pair with respect to the RF input signal. The bandwidth of a vector modulator is usually tens of megahertz [11].

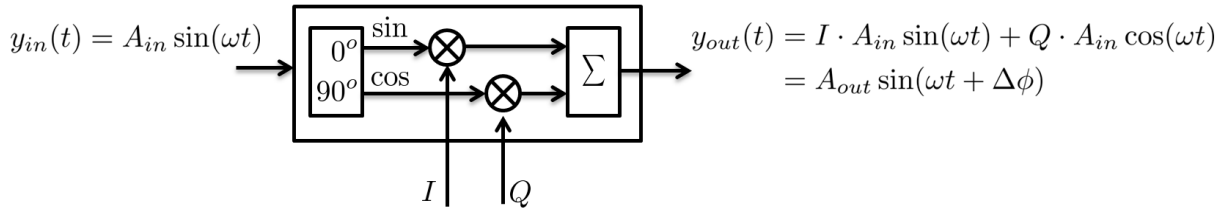


Fig. 12: Principle of vector modulator

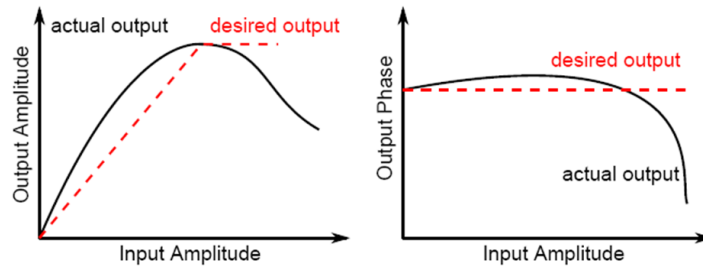


Fig. 13: Desired and real amplifier characteristics [12]

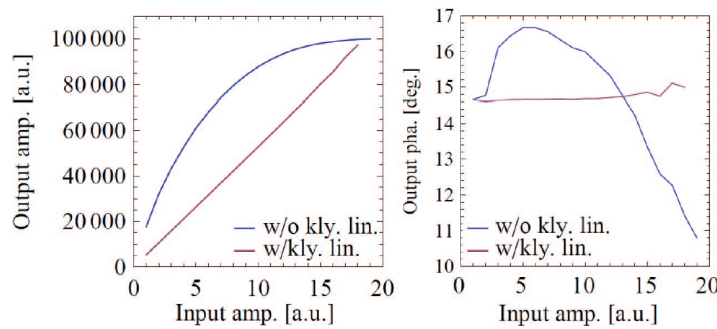


Fig. 14: Result of iSim simulation without klystron linearization (blue) and with linearization (purple). Left-hand side: klystron linearization algorithm output amplitude [arbitrary units] versus input amplitude [arbitrary units]. Right-hand side: klystron linearization algorithm output phase [degrees] versus input amplitude [arbitrary units] [12].

2.3 Amplifier

Each amplifier, e.g., a klystron, solid state amplifier, or inductive output tube, is itself a non-linear device. The non-linearity is caused by, e.g., saturation at maximum output power. Furthermore, non-linearities in terms of changes of the output amplitude and phase are mostly present if only the input amplitude is changed, see, for example, Fig. 13. For most applications, such as superconducting RF cavity control, it is sufficient to linearize the amplifier input–output (I/O) behaviour using a static I/O characteristic. An example is shown in Fig. 14, where a simulation of a real and corrected klystron characteristic is shown. The bandwidth of a klystron is of the order of 10 MHz [11]. Refer to, e.g., Ref. [12] for further details of the klystron linearization.

2.4 Cavity

This section gives a brief overview of the mathematical modelling for a TESLA-type RF cavity; detailed information can be found in Ref. [11].



Fig. 15: TESLA-type superconducting RF cavity [13]

Table 2: Parameters for superconducting RF Tesla-type cavity

Operating frequency	1.3 GHz
Length	1.036 m
Aperture diameter	70 mm
Cell to cell coupling	$\approx 2\%$
Quality factor Q_0	$\approx 10^{10}$
$r/Q := r_{\text{sh}}/Q_0$	1036 Ω

2.4.1 Introduction

A typical nine-cell TESLA-type superconducting RF cavity is shown in Fig. 15. The cavity has a length of about 1 m and is operated with a driving frequency of 1.3 GHz; its typical parameters are shown in Table 2.

2.4.2 Cavity modelling by RCL circuit

The TESLA-type superconducting RF cavity consists of nine electrically coupled cells. An equivalent RCL circuit model with nine magnetically coupled cells is shown in Fig. 16. Such a structure with nine coupled cells has nine normal modes, the so-called passband modes. The fundamental operating mode is called the π -mode, meaning that the RF fields in adjacent cells are at a phase difference of π . The closest mode to the operating mode is the $8\pi/9$ -mode, with a frequency separation of about 800 kHz. A plot of all the modes is shown in Fig. 17. Every passband mode can be modelled by an RCL circuit, which is in parallel with the others. To simplify the modelling, let's first consider only the π -mode and neglect all the other modes. Then the nine-cell structure simplifies to a single cell, displayed in Fig. 18, with generator driving term \tilde{I}_g , beam-induced driving term I_b , and an external load Z_{ext} . Here, the transmission line, circulator, and coupler are already part of the model and can be neglected. The total current going into the RCL circuit must be the same as the current inside the RCL circuit, i.e.,

$$I_C + I_{R_L} + I_L = I = \tilde{I}_g + I_b \quad (I_{R_L} = I_R + I_{Z_{\text{ext}}}, \text{ see Eq. (5)}), \quad (2)$$

using Kirchhoff's rule. Inserting the well-known relationships

$$\frac{dI_L}{dt} = \dot{I}_L = \frac{V}{L}, \quad \dot{I}_{R_L} = \frac{\dot{V}}{R_L}, \quad \text{and} \quad \dot{I}_C = C\dot{V} \quad (3)$$

leads to the differential equation for a driven RCL circuit:

$$\ddot{V}(t) + \frac{1}{R_L C} \dot{V}(t) + \frac{1}{LC} V(t) = \frac{1}{C} \dot{I}(t). \quad (4)$$

Here, the external load Z_{ext} and the cavity resistor R are combined to give the so-called loaded shunt impedance

$$R_L = \left(\frac{1}{R} + \frac{1}{Z_{\text{ext}}} \right)^{-1} = \frac{R}{1 + \beta}, \quad \text{with coupling factor} \quad \beta = \frac{R}{Z_{\text{ext}}}. \quad (5)$$

The loaded quality factor is defined similarly to the loaded shunt impedance as

$$Q_L = \left(\frac{1}{Q_0} + \frac{1}{Q_{\text{ext}}} \right)^{-1} = \frac{Q_0}{1 + \beta} \quad \left(\beta = \frac{Q_0}{Q_{\text{ext}}} \right). \quad (6)$$

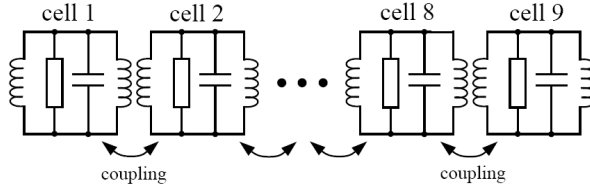


Fig. 16: Equivalent RCL circuit for nine-cell cavity modelled with nine magnetically coupled loops [11]

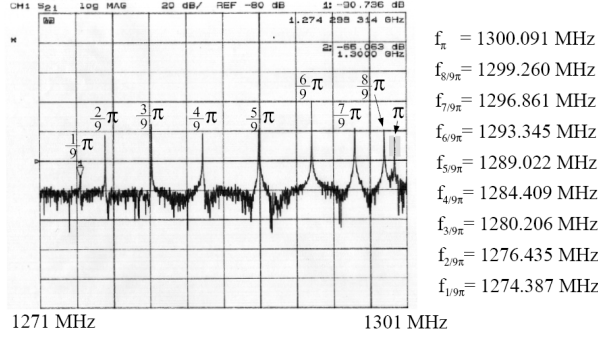


Fig. 17: Passband modes of TESLA-type nine-cell cavity [11]

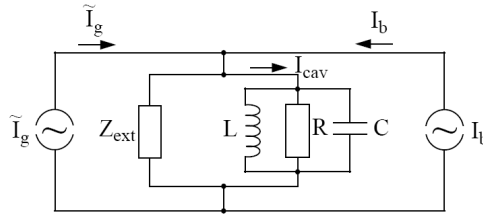


Fig. 18: Simplified equivalent RCL circuit for single-cell cavity with external load and, as driving source, generator and beam [11].

The inductance L and capacitance C can be described by the measurable cavity quantities Q_L and ω_0 with

$$\frac{1}{R_L C} = \frac{\omega_0}{Q_L} \quad \text{and} \quad \frac{1}{LC} = \omega_0^2. \tag{7}$$

Using these relations in Eq. (4) gives the well-known cavity differential equation,

$$\ddot{V}(t) + \frac{\omega_0}{Q_L} \dot{V}(t) + \omega_0^2 V(t) = \frac{\omega_0 R_L}{Q_L} \dot{I}(t), \tag{8}$$

with harmonic RF driving term $I(t) = \hat{I}_0 \sin(\omega t)$, e.g., with driving frequency $\omega = 2\pi \times 1.3$ GHz.

The solution of the cavity differential equation (Eq. (8)) for a driving term $I(t) = \hat{I}_0 \sin(\omega t)$ will be proportional to $\cos(\omega t)$. Its stationary solution, i.e., the particular solution of the cavity differential equation, is given by

$$V(t) = \hat{V}(t) \cdot \sin(\omega t + \psi) \tag{9}$$

with

$$\hat{V} = \frac{R_L \hat{I}_0}{\sqrt{1 + \tan^2(\psi)}} \approx \frac{R_L \hat{I}_0}{\sqrt{1 + (2Q_L \frac{\Delta\omega}{\omega})^2}}, \tag{10}$$

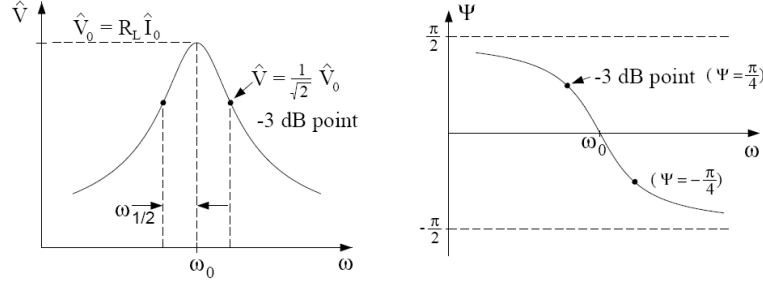


Fig. 19: Resonance curves for amplitude and phase [11]

and ψ as angle between the driving current and cavity voltage; $\psi(t) = \angle(I(t), V(t))$. Furthermore, it is shown in Ref. [11] that the tuning angle can be approximated if the generator frequency ω is very close to the cavity resonance frequency ω_0 ($\omega \approx \omega_0$) by $\tan \psi \approx 2Q_L \frac{\Delta\omega}{\omega}$, with $\Delta\omega = \omega_0 - \omega \ll \omega$. The frequency dependence of the amplitude is known as the Lorentz curve, shown in Fig. 19. The half bandwidth $\omega_{1/2}$ is defined as the frequency offset where the voltage drops to $1/\sqrt{2}$ (-3 dB) from its maximum. The corresponding phase at the -3 dB point will have an offset of 45° ($|\psi(\omega_{1/2})| = \pi/4$). The half bandwidth of a cavity is inversely proportional to the loaded quality factor Q_L and is given by:

$$\omega_{1/2} = \frac{\omega_0}{2Q_L} = \frac{1}{\tau} (\ll \omega), \quad \text{with time constant } \tau.$$

The definition of half bandwidth can be used to rewrite Eq. (10) as:

$$\ddot{V}(t) + 2\omega_{1/2}\dot{V}(t) + \omega_0^2 V(t) = \omega_{1/2} R_L \dot{I}(t). \quad (11)$$

2.4.3 Baseband model

The high-frequency part from the generator, i.e., $\sin(\omega t)$ or, more generally, $e^{j\omega t}$, is not of interest in the case of a down-conversion regulation scheme. For this reason, the high-frequency part can be separated from the slow variations using

$$\begin{aligned} V &= \vec{V}(t) e^{j\omega t}; & \vec{V}(t) &= V_I + jV_Q, \\ I &= \vec{I}(t) e^{j\omega t}; & \vec{I}(t) &= I_I + jI_Q. \end{aligned} \quad (12)$$

Consider the phasor diagram in Fig. 20. Both the driving current $\vec{I}(t)$ and the cavity voltage $\vec{V}(t)$ have the same driving frequency component ω . The cavity voltage and phase with respect to the driving current depend on the tuning angle $\psi(t)$, see Eq. (10). Inserting Eq. (12) in Eq. (11) and neglecting the second-order time derivatives of $V(t)$ leads to the first-order differential cavity equation for the envelope (cavity baseband equation) in the complex domain, as

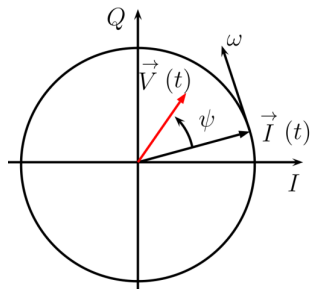
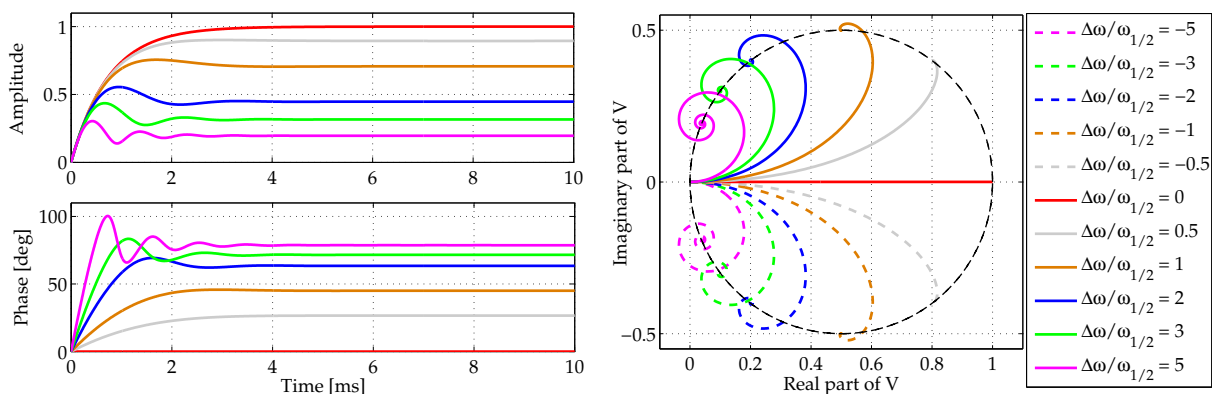
$$\dot{\vec{V}} + (\omega_{1/2} - j\Delta\omega) \vec{V} = \omega_{1/2} R_L \vec{I}. \quad (13)$$

Separating its real and imaginary parts gives the two first-order equations:

$$\begin{aligned} \dot{V}_I + \omega_{1/2} V_I + \Delta\omega V_Q &= R_L \omega_{1/2} I_I, \\ \dot{V}_Q + \omega_{1/2} V_Q - \Delta\omega V_I &= R_L \omega_{1/2} I_Q. \end{aligned} \quad (14)$$

The latter is well known in accelerator physics and can be rewritten in a so-called state space form,

$$\frac{d}{dt} \begin{bmatrix} V_I(t) \\ V_Q(t) \end{bmatrix} = \begin{bmatrix} -\omega_{1/2} & -\Delta\omega \\ \Delta\omega & -\omega_{1/2} \end{bmatrix} \begin{bmatrix} V_I(t) \\ V_Q(t) \end{bmatrix} + R_L \cdot \omega_{1/2} \begin{bmatrix} I_I(t) \\ I_Q(t) \end{bmatrix}, \quad (15)$$


Fig. 20: Phasor diagram of driving current and cavity voltage

Fig. 21: Transient step responses of a cavity for different normalized detuning values: left-hand side, shown in amplitude and phase; right-hand side, shown in complex plane.

in which V is the complex cavity voltage, I the complex driving current, $\omega_{1/2}$ the half bandwidth, $\Delta\omega = \omega_0 - \omega$ the detuning and R_L the shunt impedance of the cavity. This cavity equation has two inputs (the driving current in I and Q) and two outputs (the cavity voltage in I and Q). We will call this a multi-input, multi-output (MIMO) system.

2.4.4 Step response

Drawing the step response of Eq. (15) for different normalized detuning values $\Delta\omega/\omega_{1/2}$ for an input of which the real part is normalized to one and the imaginary part is zero, i.e., $R_L \cdot [I_I(t) \ I_Q(t)]^T = [1 \ 0]^T$, we have the graphs shown in Fig. 21. Here, the left panel of Fig. 21 shows the amplitude and phase of the resulting cavity voltage. The right panel shows the step response as a time-dependent field vector in the complex plane with the steady-state value located on the resonance circle (black dashed line), corresponding to the stationary solution in Eq. (8).

2.4.5 Additional passband modes

The latter cavity equation is given around the baseband frequency, meaning that the operating π -mode is located at frequency zero; Eq. (15) holds only for this mode. Eight other passband modes (see Fig. 17) are present for a nine-cell cavity. Thus, all the differential equations for each mode have to be added to get the overall cavity model; remember that all cavity mode models are in parallel. The field probe signal is measured at the end cell of the cavity; thus, each even mode, e.g., the $8/9\pi$ -mode, is sign-inverted such that each fundamental mode is represented in the complex domain—compare this with Eq. (13) for the π -mode—as

$$\dot{\vec{V}} + \left((\omega_{1/2})_{\frac{n}{9}\pi} - j(\Delta\omega)_{\frac{n}{9}\pi} \right) \vec{V} = (-1)^{n+1} K_{\frac{n}{9}\pi} (\omega_{1/2})_{\frac{n}{9}\pi} \cdot R_L \vec{I}, \quad n = 1, \dots, 9.$$

The extended state space form, see Eq. (15), is given as

$$\frac{d}{dt} \begin{bmatrix} V_I(t) \\ V_Q(t) \end{bmatrix} = \begin{bmatrix} -(\omega_{1/2})_{\frac{n}{9}\pi} & -\Delta\omega_{\frac{n}{9}\pi} \\ \Delta\omega_{\frac{n}{9}\pi} & -(\omega_{1/2})_{\frac{n}{9}\pi} \end{bmatrix} \begin{bmatrix} V_I(t) \\ V_Q(t) \end{bmatrix} + (-1)^{n+1} K_{\frac{n}{9}\pi} (\omega_{1/2})_{\frac{n}{9}\pi} \cdot R_L \begin{bmatrix} I_I(t) \\ I_Q(t) \end{bmatrix}. \quad (16)$$

This equation is used to compute the transfer function matrix of the π -mode ($n = 9$) with $K_\pi = 1$. The variation in the coupling and loaded quality factor for the remaining modes ($n \neq 9$) is described in Ref. [14] and requires an adjustment of static gain, bandwidth, and detuning by

$$K_{\frac{n}{9}\pi} \stackrel{n \neq 9}{=} 2 \sin^2 \left(\frac{n\pi}{18} \right), \quad (\omega_{1/2})_{\frac{n}{9}\pi} \stackrel{n \neq 9}{=} 2 \sin^2 \left(\frac{n\pi}{18} \right) \frac{\pi f_{\frac{n}{9}\pi}}{Q_L} \quad \text{and} \quad \Delta\omega_{\frac{n}{9}\pi} = 2\pi \left(f_{\frac{n}{9}\pi} - f_\pi \right), \quad (17)$$

where Q_L is the loaded quality factor and f_π is the resonance frequency of the π -mode.

2.5 Summary

In this section, we have seen the different components acting in an LLRF feedback loop. For a feedback controller design, one can follow and identify the mathematical description of each component separately. However, setting up an optimal feedback regulation of each LLRF system, e.g., 27 LLRF feedback loops at the European XFEL, requires the mathematical description and parameter estimation of a huge amount of components. To avoid this, a system modelling for all components within one step can be performed, as described in the next section.

3 System modelling

The last section gave an overview of the main components within an LLRF feedback loop, such as the vector modulator, klystron, and cavity. However, additional components are required, e.g., to transport the signal using a cable or waveguide. Mathematical modelling using, e.g., differential equations of a complete signal chain is a huge amount of work and very complex. Furthermore, consider the European XFEL project with its 27 RF stations. Each RF station will differ in its mechanical design, e.g., waveguide distribution, but also in the mathematical description of the individual components, e.g., klystron. Here, separate modelling for 27 feedback systems is required, but very time consuming. Furthermore, ageing and, e.g., temperature changes may require this modelling to optimize the feedback controller. Another way to overcome this mathematical description of each feedback loop is system modelling using a special input signal, discussed next. Such system modelling can be done in the time or frequency domain. We will see in this section why the frequency domain is the preferable approach. Furthermore, we will assume that only linear time-invariant systems are considered. These are linear systems because they are describable by linear differential equations. Time-invariance of a system implies that for any time delay $d > 0$ the response to the delayed input $u(t - d)$ is a time-delayed output $y(t - d)$. Moreover, the coefficients of the transfer function are time-invariant and their values are constant.

3.0.1 Example RCL circuit

The electrical circuit in this example (Fig. 22) contains an inductance L , a resistance R , and a capacitance C . Applying Kirchhoff's voltage law to the system, we obtain the equations:

$$L \frac{di}{dt} + Ri(t) + V_o(t) = V_i(t),$$

$$C \frac{dV_o}{dt} = i(t).$$

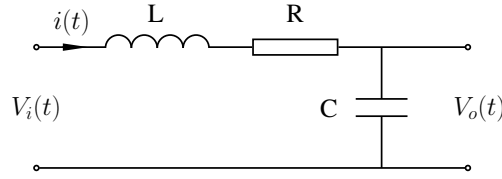


Fig. 22: Electrical RCL circuit

Eliminating the current $i(t)$ between both equations yields

$$LC \frac{d^2 V_o}{dt^2} + RC \frac{dV_o}{dt} + V_o(t) = V_i(t),$$

leading to

$$\ddot{V}_o(t) + \frac{R}{L} \dot{V}_o(t) + \frac{1}{LC} V_o(t) = \frac{1}{LC} V_i(t).$$

We can identify $V_i(t)$ with the input signal $u(t)$ and $V_o(t)$ with the output signal $y(t)$.

3.1 State space model

The previous example illustrates how dynamic systems can be modelled by a second-order linear ordinary differential equation. It may be more convenient to rewrite the differential equation in a more compact form, called a state space model, when dealing with systems that are described by higher-order differential equations. Each n th-order linear differential equation model can be transformed into a first-order vector differential equation model. Let's use the previous example and introduce a second variable as $V_m(t) = \dot{V}_o(t)$. Then we can write

$$\ddot{V}_o(t) + \frac{R}{L} \dot{V}_o(t) + \frac{1}{LC} V_o(t) = \frac{1}{LC} V_i(t)$$

as

$$\begin{aligned} \dot{V}_o(t) &= V_m(t), \\ \dot{V}_m(t) &= -\frac{R}{L} V_m(t) - \frac{1}{LC} V_o(t) + \frac{1}{LC} V_i(t). \end{aligned}$$

Defining a state vector

$$x(t) = \begin{bmatrix} V_o(t) \\ V_m(t) \end{bmatrix},$$

we can express this second-order ordinary differential equation in a more compact form as

$$\begin{bmatrix} \dot{V}_o(t) \\ \dot{V}_m(t) \end{bmatrix} = \begin{bmatrix} 0 & 1 \\ -\frac{1}{LC} & -\frac{R}{L} \end{bmatrix} \begin{bmatrix} V_o(t) \\ V_m(t) \end{bmatrix} + \begin{bmatrix} 0 \\ \frac{1}{LC} \end{bmatrix} V_i(t). \quad (18)$$

Furthermore, the output is

$$V_o(t) = \begin{bmatrix} 1 & 0 \end{bmatrix} \begin{bmatrix} V_o(t) \\ V_m(t) \end{bmatrix}. \quad (19)$$

Equations (18) and (19) are an example of a state space model, which in general has the form

$$\dot{x}(t) = Ax(t) + Bu(t), \quad (20)$$

$$y(t) = Cx(t) + Du(t), \quad (21)$$

with input $u(t)$, output $y(t)$, state $x(t)$, system matrix A , input matrix B , output matrix C , and feedthrough matrix D .

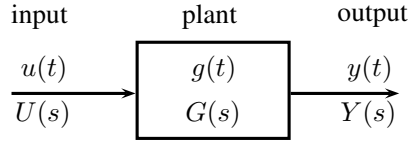


Fig. 23: System or plant $g(t)$ with input $u(t)$ and output $y(t)$; with signal notation in frequency domain using Laplace operator s .

3.2 System description in the time and frequency domains

3.2.1 Time domain

The system output $y(t)$, see Fig. 23, can be computed by a convolution of the input signal $u(t)$ with the impulse response of the system $g(t)$ as

$$y(t) = g(t) * u(t). \quad (22)$$

Solving a convolution in the time domain and, by this, analysing the system behaviour is complicated, making the system analysis very complex. Therefore, system analysis is typically done in the frequency domain.

3.2.2 Frequency domain

The system output $Y(s)$, see again Fig. 23, in the frequency domain is given as a multiplication of the transformed input signal $U(s)$ and the impulse response $G(s)$:

$$Y(s) = G(s) \cdot U(s), \quad (23)$$

with $s := \sigma + j\omega$, as operator in the frequency domain.

3.3 Transformation into the frequency domain

The transformation into the frequency domain using *Fourier transformation* is well known and given by

$$\mathcal{F}\{f(t)\} = F(\omega) = \int_{t=-\infty}^{\infty} f(t) \cdot e^{-j\omega t} dt.$$

This transformation is defined for all times, even negative times, which are not needed for system modelling. The Laplace transform, often used by system engineers, is very similar to the Fourier transform. The Fourier transform of a function is a complex function of a real variable (frequency), while the Laplace transform of a function is a complex function of a complex variable.

3.3.1 Laplace transform

Laplace transforms are usually restricted to functions of t with $t \geq 0$, with $f(t) = 0, \forall t < 0$. A consequence of this restriction is that the Laplace transform of a function is a holomorphic function of the variable $s := \sigma + j\omega$. The Laplace transform from the time to the frequency domain is given as

$$\mathcal{L}\{f(t)\} = F(s) = \int_{t=0}^{\infty} f(t) \cdot e^{-st} dt. \quad (24)$$

The Laplace transform of a signal $f(t)$ as defined in Eq. (24) exists if the integral converges. In practice, the question of existence and the region of convergence are not usually issues of concern. The *inverse Laplace transform*, mapping from the frequency to the time domain is defined as:

$$f(t) = \mathcal{L}^{-1}\{F(s)\} = \frac{1}{2\pi j} \lim_{T \rightarrow \infty} \int_{s=\alpha-jT}^{\alpha+jT} F(s) \cdot e^{st} ds.$$

We will not go into detail with the Laplace transform, since many properties and examples of using the Laplace transform can be found in the literature, e.g., Ref. [15].

3.3.1.1 Example cavity equation

The cavity equation introduced in Eq. (13) is given in the time domain as

$$\dot{\vec{V}} + (\omega_{1/2} - j\Delta\omega) \vec{V} = \omega_{1/2} R_L \vec{I} .$$

Mapping this equation into the frequency domain using the Laplace transform is done by solving Eq. (24) or by using the relations given in Table 3. Here, the cavity equation in the frequency domain is given as

$$\begin{aligned} s\vec{V} + (\omega_{1/2} - j\Delta\omega) \vec{V} &= \omega_{1/2} R_L \vec{I} , \\ (s + (\omega_{1/2} - j\Delta\omega)) \vec{V} &= \omega_{1/2} R_L \vec{I} , \end{aligned}$$

where only the first derivative in time is transformed using No 5 from Table 3 and setting $f(0) = 0$. Sorting the input (\vec{I}) and output (\vec{V}) of the system leads to the transfer function $G(s)$, defined as the ratio of the output to the input signal, as:

$$\begin{aligned} \vec{V}(s) &= \frac{\omega_{1/2} R_L}{s + (\omega_{1/2} - j\Delta\omega)} \cdot \vec{I}(s) \\ G(s) &= \frac{\vec{V}(s)}{\vec{I}(s)} = \frac{\omega_{1/2} R_L}{s + (\omega_{1/2} - j\Delta\omega)} . \end{aligned}$$

This concept is shown in Fig. 23. If we consider the non-complex MIMO case from Eq. (14), with

$$\begin{aligned} \dot{V}_I + \omega_{1/2} V_I + \Delta\omega V_Q &= R_L \omega_{1/2} I_I , \\ \dot{V}_Q + \omega_{1/2} V_Q - \Delta\omega V_I &= R_L \omega_{1/2} I_Q , \end{aligned}$$

and if we assume that $\Delta\omega = 0$, i.e., there is no coupling between the I and Q channels, we get

$$\begin{aligned} \dot{V}_I + \omega_{1/2} V_I &= R_L \omega_{1/2} I_I , \\ \dot{V}_Q + \omega_{1/2} V_Q &= R_L \omega_{1/2} I_Q , \end{aligned}$$

leading to two decoupled first-order single-input, single-output (SISO) systems as

$$G_{II}(s) = G_{QQ}(s) = \frac{V_x}{I_x} = \frac{R_L \omega_{1/2}}{s + \omega_{1/2}} ,$$

with x as $*_{II}$ or $*_{QQ}$. Based on this transformation, we can directly find several properties of a first-order transfer function given as

$$G(s) = \frac{b_0}{s + a_0} ,$$

such as the *static gain*, given as $K_P = b_0/a_0$ for $s \rightarrow 0$, the *time constant*, as $\tau = 1/a_0$, and the *step response in time*, as $y(t) = K_P(1 - e^{-t/\tau})$; these properties are displayed in Fig. 24.

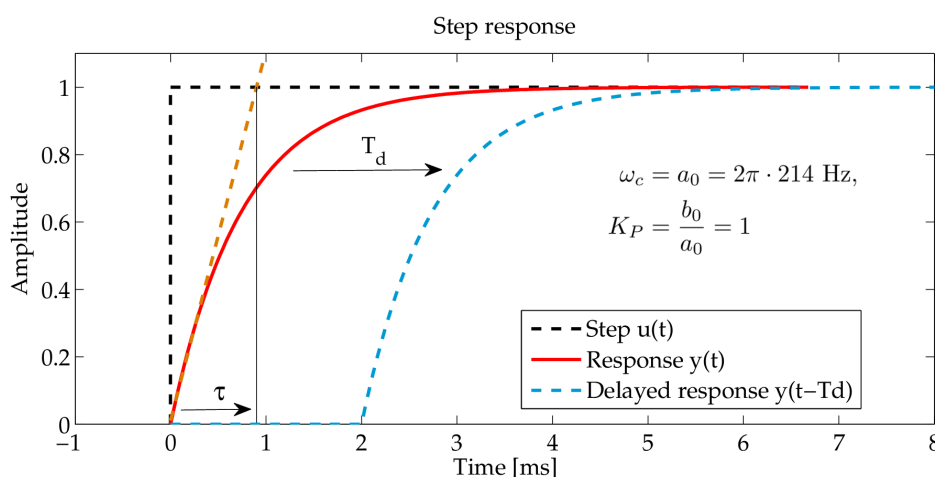
3.3.1.2 Time delay

A positive time delay within the system shifts the output signal by the delay. Such a time-delayed system can be described by a system free of time delay $G(s)$ and the delay. The overall system including the time delay T_d is hereby given as

$$G_d(s) = G(s) \cdot e^{-T_d \cdot s} .$$

Table 3: Examples of Laplace transforms

No	Time domain $f(t)$	Frequency domain $F(s)$
1	Unit impulse $\delta(t)$	1
2	Unit step $\sigma(t)$	$\frac{1}{s}$
3	t	$\frac{1}{s^2}$
4	t^n	$\frac{n!}{s^{n+1}}$
5	$\frac{df}{dt} = \dot{f}(t)$	$sF(s) - f(0)$
6	$f''(t)$	$s^2F(s) - sf(0) - f'(0)$
7	e^{at}	$\frac{1}{s-a}; s > a$
8	$t^n e^{at}$	$\frac{n!}{(s-a)^{n+1}}; s > a$
9	$\sin at$	$\frac{a}{s^2+a^2}; s > 0$
10	$\cos at$	$\frac{s}{s^2+a^2}; s > 0$
...

**Fig. 24:** Step response of first-order system: time delay, $T_d = 2 \text{ ms}$

3.3.1.3 Bode diagram

The information about the frequency response can be displayed graphically. The most widely used graphical representation of a frequency response is the Bode diagram. The magnitude and phase are plotted versus frequency in two separate plots, where a log scale is used for magnitude and frequency and a linear scale for the phase. The magnitude and phase are defined as

$$|G(s)|_{\text{dB}} = 20 \log_{10}(|G(s = j\omega)|) \quad \text{and} \quad \angle(G(s)) = \arg(G(s = j\omega)).$$

Consider a system given with a measurable input $u(t)$ and output $y(t)$. Apply to the input a sinusoidal signal with amplitude set as 1 and frequency f_i as $u(t) = \sin(2\pi f_i t)$. This leads to an output signal $y(t) = K \cdot \sin(2\pi f_i t + \varphi)$, where the amplitude and phase of the sinusoidal frequency may change. The input/output gain and phase relation between input and output signal for all frequencies f_i results in a Bode diagram. An example of a Bode diagram is given in Fig. 25. This Bode diagram shows the delay-free system $G(s)$, the pure time delay $\exp(-T_d s)$, and its combination as serial connection, $G(s) \cdot \exp(-T_d s)$. Here, it can be seen that the log scale is useful because the transfer function is composed of pole and zero factors that can be added graphically, i.e., adding $G(s)$ and $\exp(-T_d s)$ leads to the combined transfer function. Again, the static gain ($f \rightarrow 0$) and the corner frequency (-3 dB drop at 214 Hz) can be read out. Furthermore, it is shown that a pure time delay has no effect on the magnitude given as $|e^{-T_d s}| = 1$, i.e., only the output is delayed without change in the gain. The phase of a pure time delay shows a roll-off

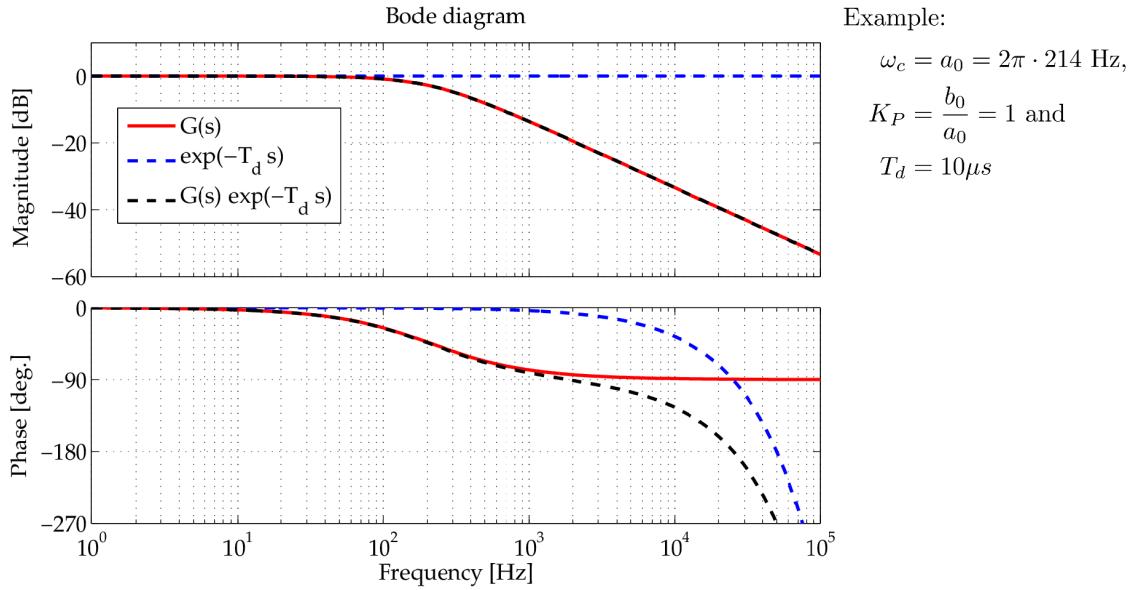


Fig. 25: Bode diagram of example system without and with time delay

of

$$\begin{aligned} \angle(e^{-T_d \cdot s}) &= \varphi(\omega) = -T_d \omega \quad [\text{rad}] \\ &= -T_d \omega \frac{180}{\pi} \quad [\text{deg}]. \end{aligned}$$

3.3.1.4 Example Bode diagram for cavity model

Figure 26 shows the resulting continuous-time white-box model for the cavity with all fundamental modes. Here, it is assumed that the cavity equation includes an initial detuning of $\Delta\omega_\pi = -2\pi \cdot 10 \text{ Hz}$ and a loaded quality factor of $Q_L = 3 \times 10^6$. The Bode diagram is computed by Eqs. (16) and (17).

3.4 System connection

If not just one system but several systems are considered, it may required to connect them using a serial and parallel connection or in a feedback scheme.

3.4.1 Serial connection

The serial connection of two systems is simply the multiplication of the individual systems, shown in Fig. 27.

3.4.2 Parallel connection

The parallel connection of two systems is the sum of the systems, resulting in a combined system, Fig. 28.

3.4.3 Feedback

In contrast with a serial and parallel connection, a positive feedback loop, indicated by a summation of the feedback path from $G_2(s)$ to the input of the system $G_1(s)$, leads to a combined system with a forward path divided by one minus the loop path, i.e., in this example the serial connection of $G_1(s)$ and $G_2(s)$, Fig. 29. For a negative feedback loop, used for most of the feedback controller, the sign of the denominator needs to be changed from minus to plus.

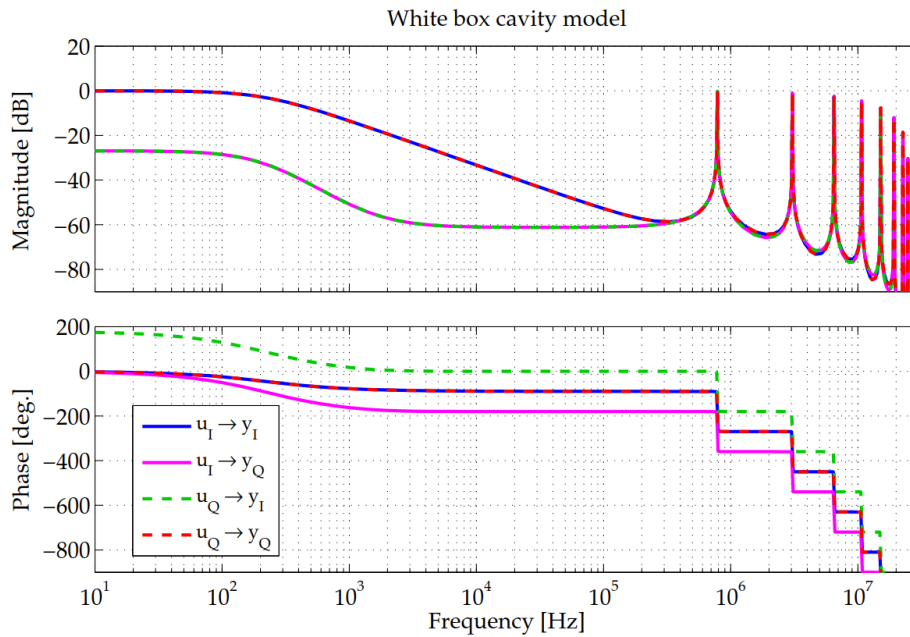


Fig. 26: Continuous-time cavity baseband white-box model without time delay. The fundamental π -mode ($f_\pi = 1.3$ GHz) is located at frequency zero. The other peaks are the eight additional fundamental cavity modes, i.e., from $8\pi/9$ -mode to $1\pi/9$ -mode.

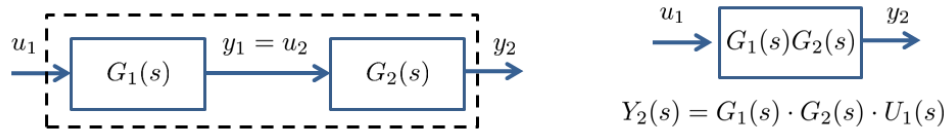


Fig. 27: Serial connection of two systems



Fig. 28: Parallel connection of two systems

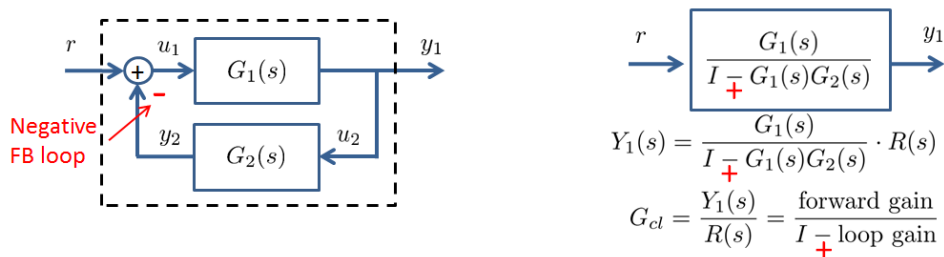


Fig. 29: Feedback of two systems

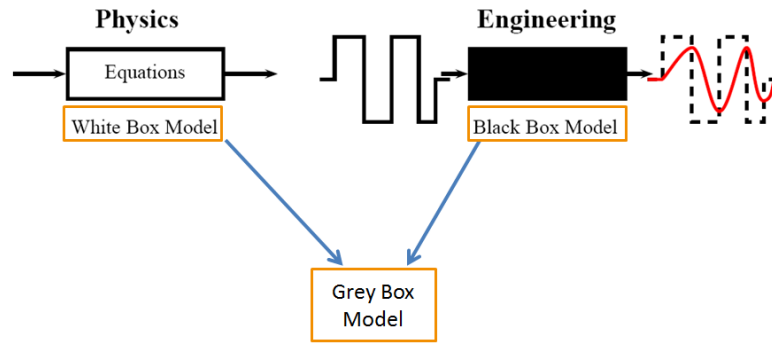


Fig. 30: Overview of system modelling

3.4.4 Summary

We have considered the system description using input/output signals of individual subsystems. The combination of different systems with different paths is shown in Section 3.4. In the next section, we will focus on the identification of a system model by exciting a system with special input signals and observing its output response.

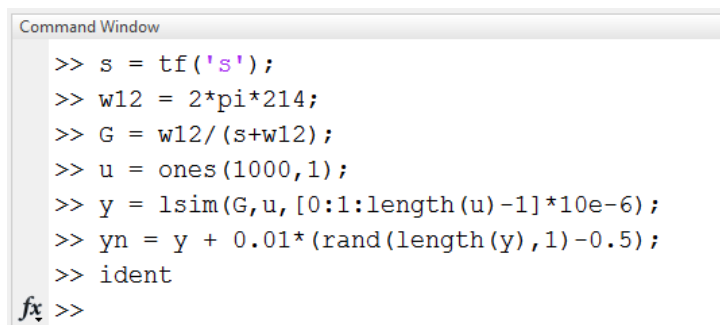
3.5 System identification

A system model is a simplified representation or abstraction of a reality. Modelling the reality is generally too complex to produce an exact copy. Furthermore, much of the complexity is actually irrelevant in problem solving, e.g., controller design. This can be overcome to define a robust controller that can cope with model uncertainties. In general, one can describe a system using different approaches. On the one hand, a mathematical description can be created, using differential equations. This is a so-called *white-box model*, where all necessary components are described, e.g., the cavity modelling described in Section 2.4, which is already an example of the *white-box modelling* approach. On the other hand, system engineers often use so-called *black-box models*, where no assumption about the system is made, see Fig. 30. Applying special input signals, e.g., pseudo-random binary signals, and observing the output signal leads to the possibility of estimating the system impulse response, i.e., the transfer function in the frequency domain or the state space model in the time domain. A combination of white-box and black-box modelling is often used to define the main physical equations describing a system. A *grey-box model* can be identified by leaving important parameters within those main equations of the white-box model as free parameters to be identified. The main possibilities of a system identification and its different approaches to identify a system are described in Ref. [16]. An example of a grey-box modelling approach to identify a superconducting RF feedback loop can be found in Ref. [17].

In the following, a short example of a black-box modelling using MATLAB is given. For the modelling, MATLAB provides a graphical tool within the *System Identification Toolbox*TM. This tool allows the transfer function, state space models, etc., to be identified only for SISO systems. Estimation of MIMO systems requires use of the command line.

Let's define a transfer function (tf command) of a system $G(s)$, its input signal $u(t)$, which is a step, and an output signal, which is the simulation of the input with the system using the MATLAB `lsim` command, see Fig. 31. To this output signal, 1% noise is added by a random signal generator. The MATLAB `ident` command opens a graphical interface for SISO system identification, see Fig. 32. Within this graphical tool, the following steps need to be taken.

1. Import data.
 - Choose data format and select the input and output data.
 - *Hint: An example data-set should be available.*



```

Command Window
>> s = tf('s');
>> w12 = 2*pi*214;
>> G = w12/(s+w12);
>> u = ones(1000,1);
>> y = lsim(G,u,[0:1:length(u)-1]*10e-6);
>> yn = y + 0.01*(rand(length(y),1)-0.5);
>> ident
fx >>

```

Fig. 31: MATLAB command line to define system identification

- Adjust the sampling interval.
2. Estimate the system model.
 - Select one of the proposed methods, e.g., transfer function, state space model.
 - Define the number of poles and zeros.
 - Choose continuous or discrete time for the resulting model.
 - If necessary, set the I/O delay.
 3. Compare the model (tf1) with the plant G.
 - *Hint: You can import the initial plant model G for comparison.*
 4. Export the system model to the workspace for further use of the dataset, e.g., controller design.

This graphical tool gives an idea of how system identification using MATLAB works. Without going into detail, the identification requires some knowledge of the plant, to avoid the identification of unnecessary dynamics of the system using an overestimated model order. As a rule of thumb, start with a low system order and increase the model order (number of poles and zeros) until the system response fits the simulated model response sufficiently well. Another method to estimate the minimum model order is to use the state space model as the resulting model and choose the option *Pick best value in the range*. This option guessing the optimal model order based on the I/O data.

The interested reader is referred to other books and publications for detailed information of the systems identification.

4 Feedback controller design

We will start in this section with an overview of the different regulation or control schemes and their usage before defining the objective of a feedback control problem. Since each feedback scheme changes the transfer function (poles and zeros) of the closed loop, it is further necessary to introduce some checks for the stability of the resulting system.

4.1 Ways to control

There are different ways to control a plant or system. On the one hand, there is the open-loop case, Fig. 33, and on the other hand, regulation using a feedback loop, Fig. 34. If the disturbance acting on the plant is known, using only a feedforward adaptation scheme, Fig. 35, or using a feedforward control scheme for the reference and disturbance together with feedback control, Fig. 36, are further ways to minimize disturbances.

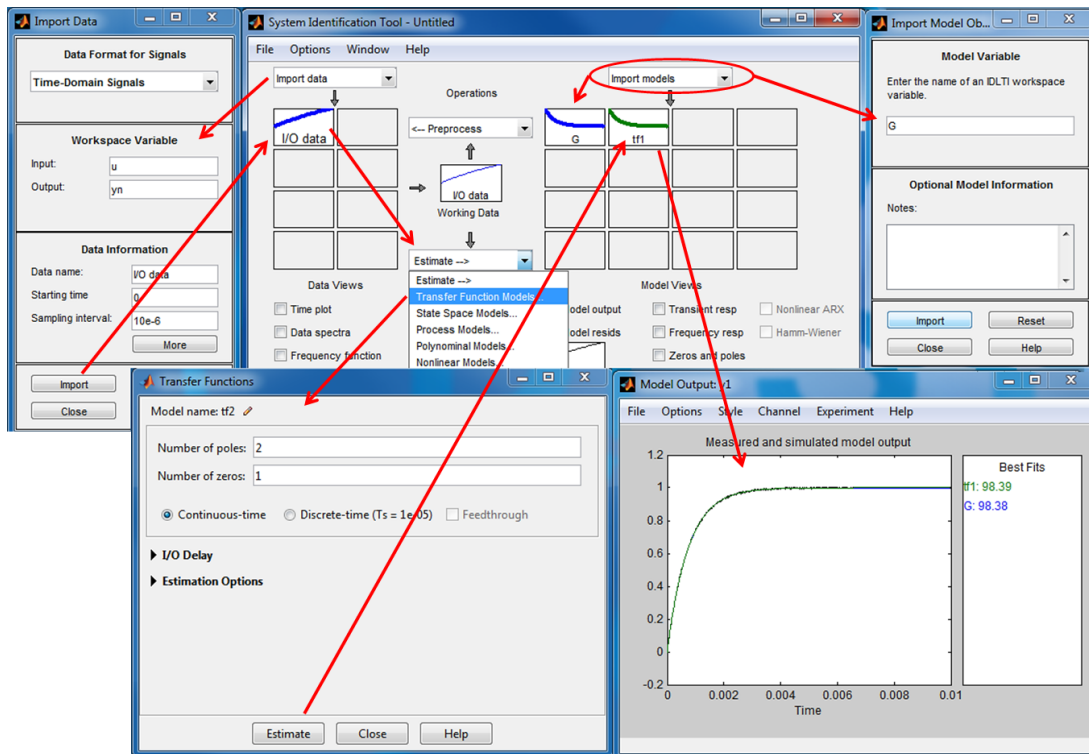


Fig. 32: System identification tool in MATLAB

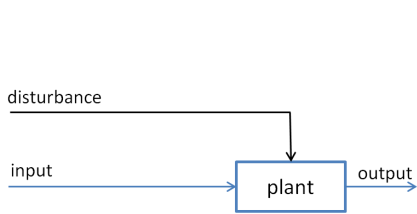


Fig. 33: Open-loop scheme

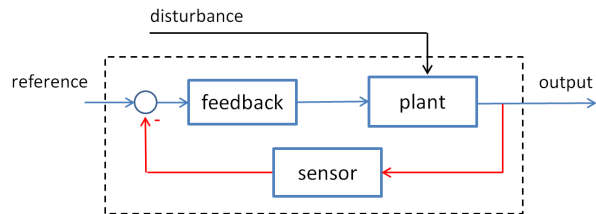


Fig. 34: Feedback scheme

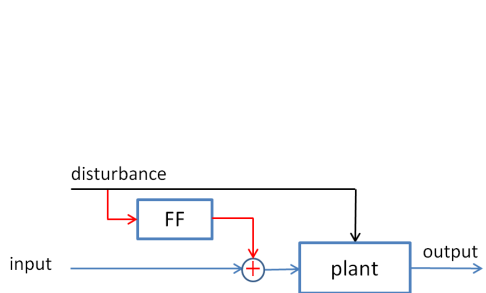


Fig. 35: Feedforward scheme

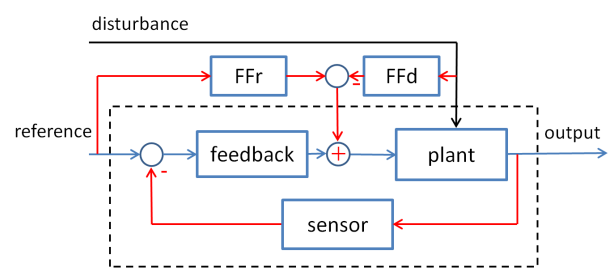


Fig. 36: Feedback scheme with feedforward compensation

4.1.1 Open loop

The input/output (I/O) behaviour of a system driven in open loop needs to be known exactly, since there is no feedback to adjust the input signal to compensate for output variations e.g., caused by disturbances. Such a scheme can be used if the output signal is not critical and may change by several per cent without losing system performance.

4.1.2 Feedforward scheme

Like the open-loop case, a precise knowledge of I/O behaviour is required when operating a system in a feedforward scheme. The disturbances must be measurable and therefore they can be compensated for by adjusting the drive signal. However, in the feedforward scheme, there is no process for automatically adjusting the output signal to be controlled.

4.1.3 Feedback scheme

The signal to be controlled (output) is fed back using a feedback regulation scheme. Therefore, the output signal acts directly on the input. In contrast with the feedforward scheme, this interconnection of signals changes the system transfer function, as seen in Section 3.4.

4.1.4 Feedback controller together with feedforward scheme

This control structure is often called a two-degrees-of-freedom controller, where two signals, i.e., the output and reference, are treated independently by introducing, in addition to a feedback controller, a feedforward controller to the reference (FFr). Furthermore, a feedforward controller for the measurable disturbance is used. Hence, this concept copes with a combination of the feedback and the two feedforward controllers.

4.1.5 Short summary

The optimal regulation approach depends on the application for which it is used. Here, several questions must be addressed, e.g., are the signals of interest or even all signals measurable or observable? Further information on the different regulation schemes can be found, e.g., in Ref. [18] or control theory lectures from universities.

4.1.5.1 Example feedback loop for cavities

Figure 37 depicts an example of a feedback loop in LLRF controls. The plant consists in this case of a serial connection of its main components, i.e., the pre-amplifier, klystron, and cavity. The signal to be controlled is depicted as an ideal signal $y_i(t)$, while, in practice, disturbances to the output $d_y(t)$ need to be added. The measurable signal $y_r(r)$ is overlapped with noise $n(t)$ from the detection scheme. The feedback controller with the error signal as input, i.e., the difference between the reference $r(t)$ and the measured output signal $y_r(t) + n(t)$, optimizes the ideal drive signal $u_i(t)$. Again, we can assume that the drive signal to the real plant is modulated by a disturbance $d_u(t)$ leading to the real drive signal $u_r(t)$, which is the input to the plant. To complete the entire feedback loop, several time delays in the detection path, the controller, and plant must be added; these are not negligible and affect the feedback operation.

4.2 Objective of a feedback control problem

The main objective of a feedback regulation scheme is to make the output $y(t)$ behave in a desired way by manipulating the plant input $u(t)$. Two different scenarios can be considered.

1. Regulator problem (output disturbance rejection with constant reference);
2. Servo problem (reference tracking without disturbance).

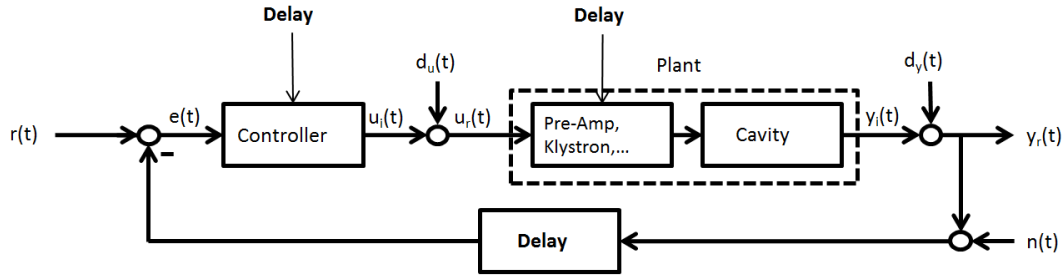


Fig. 37: Simplified block diagram of cavity feedback loop with signals and subsystems to be considered

On the one hand, in the *regulator problem*, the main goal is to suppress output disturbances. Here, it is assumed that the reference signal is constant and the feedback loop counteracts only the effect of disturbances. On the other hand, in the *servo problem*, the reference signal must be tracked optimally. In this case, it is assumed that no disturbance acts on the plant. Therefore, the goal is to keep the output close to the reference by manipulating the plant input.

Mostly, the regulator problem is addressed in practice. However, for both cases, the error signal, which is the difference between reference and output, should be minimal.

4.3 Stability

A system is stable if, for a given bounded input signal, the output signal is bounded and finite (bounded input, bounded output stable); otherwise, the system is called unstable. Stability can be checked for stable and unstable linear systems in open or closed feedback loops. For an unstable open-loop system, the main goal is to stabilize the closed-loop system behaviour using a feedback controller. The stability can be checked in the time or frequency domain.

4.3.1 Time domain

The system is stable if its impulse response $g(t)$ is absolutely integrable and bounded:

$$\int_{t=-\infty}^{\infty} |g(t)| dt < \infty .$$

This stability check in the time domain is often not preferred and frequency domain checks are recommended.

4.3.2 Frequency domain

The stability can be checked in the frequency domain using:

1. pole location (all poles in left half plane);
2. Bode diagram;
3. Nyquist plot;
4. H -infinity norm (mostly for MIMO systems);
5. harmonic balance (for non-linear systems).

In the following, we will restrict the stability check to SISO systems, i.e., cases (1) to (3). The interested reader is referred to, e.g., Ref. [18] to learn about MIMO stability checks using the H -infinity norm. Furthermore, special methods, e.g., the harmonic balance, exist to check the stability for non-linear systems, which are beyond the scope of this paper.

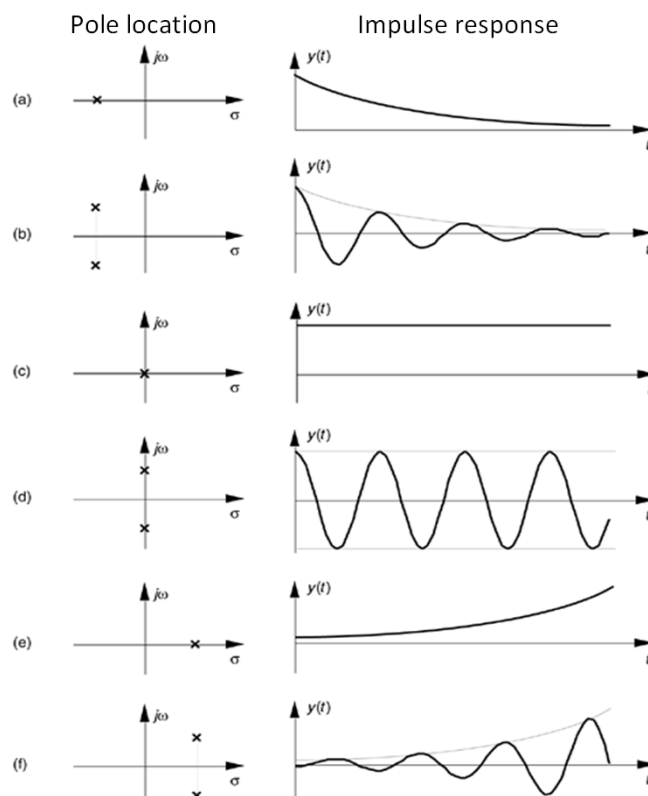


Fig. 38: Time-domain impulse response for different pole locations [19]

4.3.2.1 Pole location

Assume a SISO continuous-time transfer function of the system given as

$$G(s) = \frac{b_m s^m + b_{m-1} s^{m-1} + \dots + b_1 s + b_0}{a_n s^n + a_{n-1} s^{n-1} + \dots + a_1 s + a_0}.$$

This system has n poles and m zeros, and if it is physically realizable, we have $n \geq m$. The values of s at which the denominator of $G(s)$ takes the value zero, and therefore at which $G(s)$ becomes infinite, are called the poles of the transfer function $G(s)$. The locations of the poles in the complex plane determine the dynamic behaviour of the system; for this reason the denominator polynomial of the transfer function is called the characteristic polynomial. To check the stability, the poles of the system must be computed and its pole location must be checked. If all poles have negative real part and therefore lie in the left half plane of the complex plane, the system is stable. A system is called semi-stable if the real part of a pole is zero. A visualization is given in Fig. 38 as an example.

4.3.2.2 Bode diagram and Nyquist plot

Another way of checking the stability of the system is by its Bode magnitude and phase plot or by its corresponding Nyquist representation. The Nyquist plot is simply the mapping from the Bode amplitude and phase plot to the complex plane; here, the frequency information is lost. The following description is a very simplified check; for further details, the reader is referred to, e.g., Ref. [18].

The system is plotted in open loop and the so-called gain margin and phase margin can be read from the graph. This gives an easy stability check for the closed-loop system using a proportional controller. Hence, both checks are made in open loop, and the closed-loop stability can be predicted.

Example: Assume a proportional controller connected serially with the system and plot the system as a Bode diagram or a Nyquist plot, as shown in Figs. 39 and 40, respectively. Read out the *phase margin*

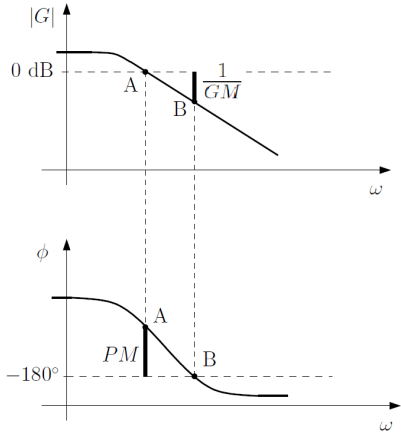


Fig. 39: Bode: gain and phase margin

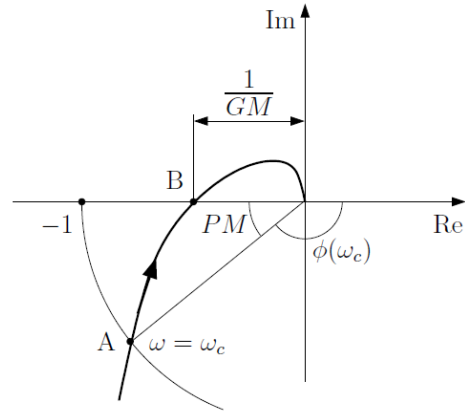


Fig. 40: Nyquist: gain and phase margin

at point A, where the magnitude crosses 0 dB and the *gain margin* at point B, where the phase crosses -180° . Increasing the proportional controller gain from one shifts the point A towards higher frequencies for the Bode representation. This obviously reduces the phase margin. If points A and B are equal, i.e., if the controller gain is equal to the reciprocal of the gain margin, from the system Bode plot, the closed-loop system becomes unstable, i.e., with a phase shift of 180° , the negative feedback loop becomes a positive feedback loop. The same can be observed using the Nyquist plot. Here, the complex system line is blown up and the point B moves towards the critical point -1 , i.e., with magnitude 0 dB and phase -180° in the Bode plot. Furthermore, point A moves on the circle with radius 1 towards -1 causing a decrease of the phase margin.

Thus, both representations help to identify the maximum possible proportional feedback gain. Furthermore, one can easily see whether the loop is stable or not. To err on the side of caution in real applications, it is often recommended to choose a phase margin of 60° to cope with system variations and to keep the closed-loop operation more robust.

4.3.2.3 MIMO system stability check

Consider a MIMO system with transfer matrix $G_{cl}(s)$ with input $r(t)$ and output $y(t)$ operated in a closed feedback loop, see e.g., the example given in Fig. 29. This feedback system is stable if and only if the transfer function matrix $G_{cl}(s)$ is stable. Furthermore, it is mandatory that each transfer function itself within the transfer matrix is stable. Furthermore, the MIMO stability can be checked using the generalized Nyquist plot or H -infinity based methods, see, e.g., Ref. [18].

4.4 Gang of four

Often it is not sufficient to check the stability or closed-loop behaviour for only one I/O pair. It is highly recommended to check it for the so-called *gang of four*. An example of a feedback loop is depicted in Fig. 41. Here, the system has one output ($y(t)$), three inputs ($r(t)$, $d(t)$, $n(t)$), and intermediate signals (e.g., $e(t)$ and $u(t)$). First check the response of $y(t)$ to disturbance $d(t)$ and the response of $u(t)$ to measurement noise $n(t)$ by

$$G_{yd}(s) = \frac{G(s)}{1 + G(s)C(s)} \quad \text{and} \quad G_{un}(s) = -\frac{C(s)}{1 + G(s)C(s)}.$$

This is followed by a check of the robustness to process variations by

$$S(s) = \frac{1}{1 + G(s)C(s)} \quad \text{and} \quad T(s) = \frac{G(s)C(s)}{1 + G(s)C(s)},$$

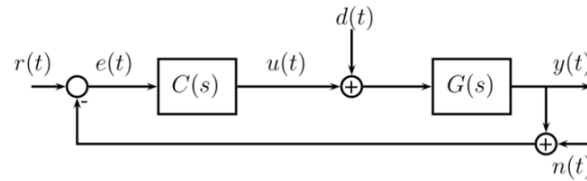


Fig. 41: Closed loop with feedback controller $C(s)$ and plant $G(s)$ operated in negative feedback loop. The main signals are given: reference $r(t)$, output $y(t)$, error $e(t)$, controller output $u(t)$, disturbance $d(t)$, and noise $n(t)$.

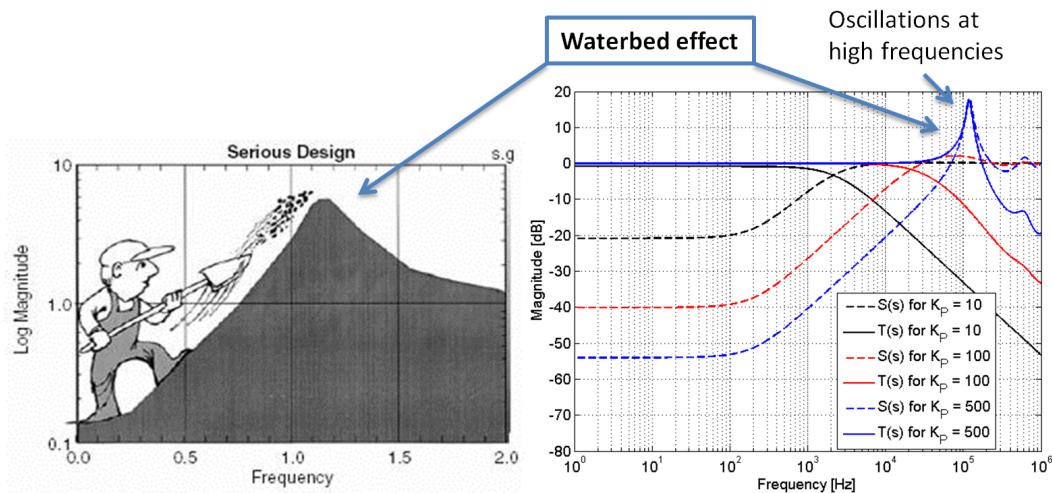


Fig. 42: Increase of feedback gain and the *waterbed effect* [20]

where $S(s)$ is the so-called sensitivity function and $T(s)$ is the so-called complementary sensitivity function. Both transfer functions depend on the loop transfer function $L(s) = G(s) \cdot C(s)$. The coupling between the sensitivity and complementary sensitivity function is given for the SISO case as $S(s) + T(s) = 1$. In a typical feedback operation $S(s)$, for frequencies towards zero should be small ($S(0) \rightarrow 0$) and $S(\infty) \rightarrow 1$, i.e., often referred to as disturbance rejection, and $T(0) \rightarrow 1$ and $T(\infty) \rightarrow 0$, i.e., referred to as reference tracking. By changing the controller transfer function $C(s)$, all four transfer functions to be checked for stability and its behaviour are changing. The effect of changing the controller gain is often visualized by $S(s)$ and $T(s)$; an example is given in Fig. 42. Pushing down the sensitivity function $S(s)$ for low frequencies pushes up $S(s)$ for higher frequencies caused by the so-called waterbed effect. In this way, high-frequency oscillations occur if the controller gain is increased. Hence, the optimal feedback strategy is often not reaching high feedback gain. The optimal controller is often a trade-off between reference tracking and disturbance rejection.

Hint: By using, in addition, a filter function for the reference, the so-called *gang of six* is formed, so, in total, six transfer functions need to be checked.

4.5 Types of feedback controller design

A feedback controller can be designed in two different ways, i.e., in the frequency or time domain. The *classical feedback controller design* is normally implemented in the frequency domain for a SISO controller design using loop-shaping techniques. Here, the open-loop controller and system analysis is performed using e.g., Bode or Nyquist plots, see Section 4.3.2. A simple example is the PID controller with transfer function

$$\frac{U(s)}{E(s)} = C(s)$$

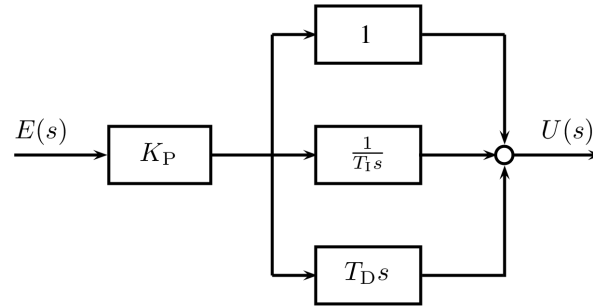


Fig. 43: PID controller

and the error signal as input, i.e., the difference between the set-point and the signal to be controlled, and the output signal, i.e., the signal driving the system or plant. Its time and frequency response is given as

$$\begin{aligned}
 u(t) &= K_P \left(e(t) + \frac{1}{T_I} \int_{t_0}^t e(\tau) d\tau + T_D \frac{de(t)}{dt} \right), \\
 &= K_P e(t) + K_I \int_{t_0}^t e(\tau) d\tau + K_D \dot{e}(t), \\
 U(s) &= K_P E(s) + \frac{1}{s} K_I E(s) + s K_D E(s), \\
 &= K_P \left[1 + \frac{1}{T_I s} + T_D s \right] E(s),
 \end{aligned}$$

with a block diagram for the frequency domain depicted in Fig. 43. The proportional part accounts for present values of the error, i.e., for a positive proportional gain, and if the error is positive, the control output will also be positive. The integral part accounts for past values of the error. Therefore, the integral of the error will accumulate over time and the controller will respond by applying a stronger action. The derivative part accounts for possible future trends of the error, based on its current rate of change.

A PID controller relies only on the measured process variable, not on knowledge of the underlying process. The use of the PID algorithm does not guarantee optimal control of the system, or even its stability. Normally PI controllers are in use, since the derivative action is sensitive to measurement noise (for digital signal processing this involves analogue-to-digital converter noise), whereas the absence of an integral term may prevent the system from reaching its target value. Here, the goal is to tune two parameters (K_P and K_I) to achieve a kind of optimal closed-loop behaviour. The tuning of a PID controller in general can be implemented in different ways, e.g., loop-shaping techniques, manual tuning by observing the closed-loop behaviour, or the Ziegler–Nichols tuning rules. The interested reader is referred to the literature for more detail on such tuning rules.

In contrast with classical feedback control, the *modern feedback controller design* is usually implemented as time-domain analysis, i.e., the system is presented as a state space model, given as

$$\begin{aligned}
 \dot{x}(t) &= Ax(t) + Bu(t), \\
 y(t) &= Cx(t) + Du(t).
 \end{aligned}$$

Such a system representation and, therefore, the modern feedback controller design is not restricted to SISO systems. Hence, it is more general for MIMO systems and often based on signals directly, e.g., the linear quadratic regulator, or closed-loop shaping methods, e.g., considering the H -infinity norm of the weighted sensitivity function. The *linear quadratic regulator control* approach assumes that the plant dynamics are linear and known. The quadratic cost function is given as

$$J = \int_0^{\infty} [x(t)^T Q x(t) + u(t)^T R u(t)] dt, \quad (25)$$

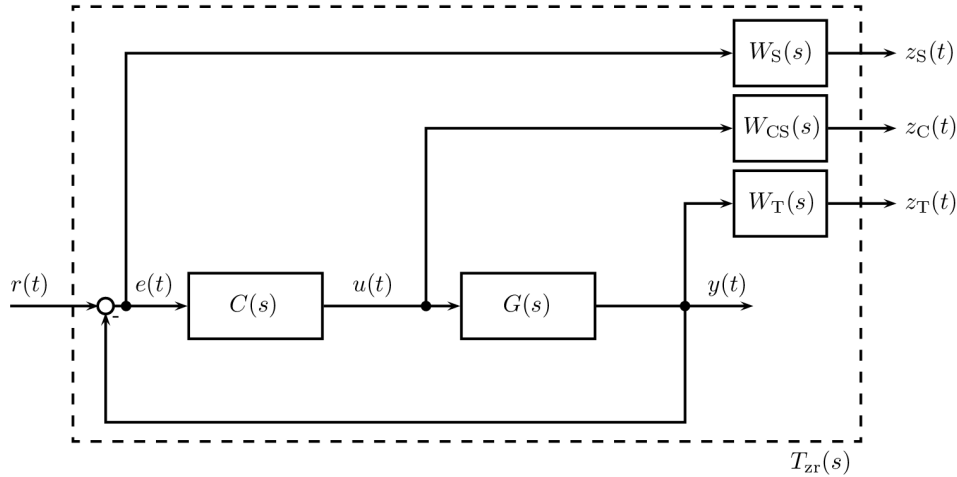


Fig. 44: H_∞ design problem with shaping filter $W_S(s)$, $W_{CS}(s)$, and $W_T(s)$

with weighted state $x(t)$ and weighted controller output $u(t)$; the constant weighting matrices Q and R are the design parameters. The optimal solution to this problem is

$$u(t) = -K \cdot x(t),$$

with $K = R^{-1}B^T X$ and X as the unique positive semi-definite solution of the Riccati equation

$$A^T X + XA - XBR^{-1}B^T X + Q = 0.$$

Often not all states $x(t)$ are directly measurable, a prerequisite for linear quadratic regulator state feedback. This requires a Kalman filter as state estimator and its regulation on the estimated state. The reader is referred to Ref. [18].

In contrast with state feedback using a linear quadratic regulator, direct feedback to the measurable output signal $y(t)$ can be designed, e.g., using H -infinity (H_∞) based optimization methods and weighting filter functions to shape the sensitivity and complementary sensitivity function, see Section 4.4. A block diagram is given in Fig. 44. Here, the goal is to find the optimal controller minimizing the H_∞ -norm

$$\|T_{zr}(s)\|_\infty = \left\| \left[\begin{array}{c} W_S(s) \cdot S(s) \\ W_{CS}(s) \cdot C(s)S(s) \\ W_T(s) \cdot T(s) \end{array} \right] \right\|_\infty < 1 \quad (26)$$

from the reference $r(t)$ to the fictitious output signals $z(t)$, which are connected by shaping filters to different signals within the feedback loop. Keeping the H_∞ -norm below 1 one guarantees a stable closed-loop system, see the small-gain theorem. A complete description of the H_∞ -norm optimization would be beyond the scope of this paper and the interested reader is referred to Ref. [18].

5 Examples

Next, some examples for feedback controller design at different facilities are given. First let's start with the feedback controller design for an RF field regulation, where the system is operated in pulsed mode. The transition from pulsed to continuous wave mode often requires an increase in Q_L , putting additional effort in microphonics suppression or rejection acting to the cavities, described in the second example. If additional disturbances are measurable, a feedback scheme based on known disturbance is recommended, discussed in the last example.

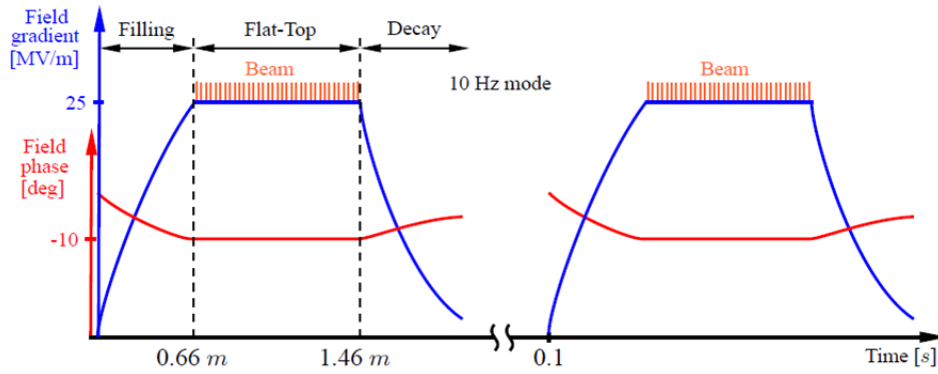


Fig. 45: Pulsed mode at FLASH with filling, flattop, and decay. The electron bunches are injected during the flattop time, where the amplitude and phase of the RF field needs to be kept constant.

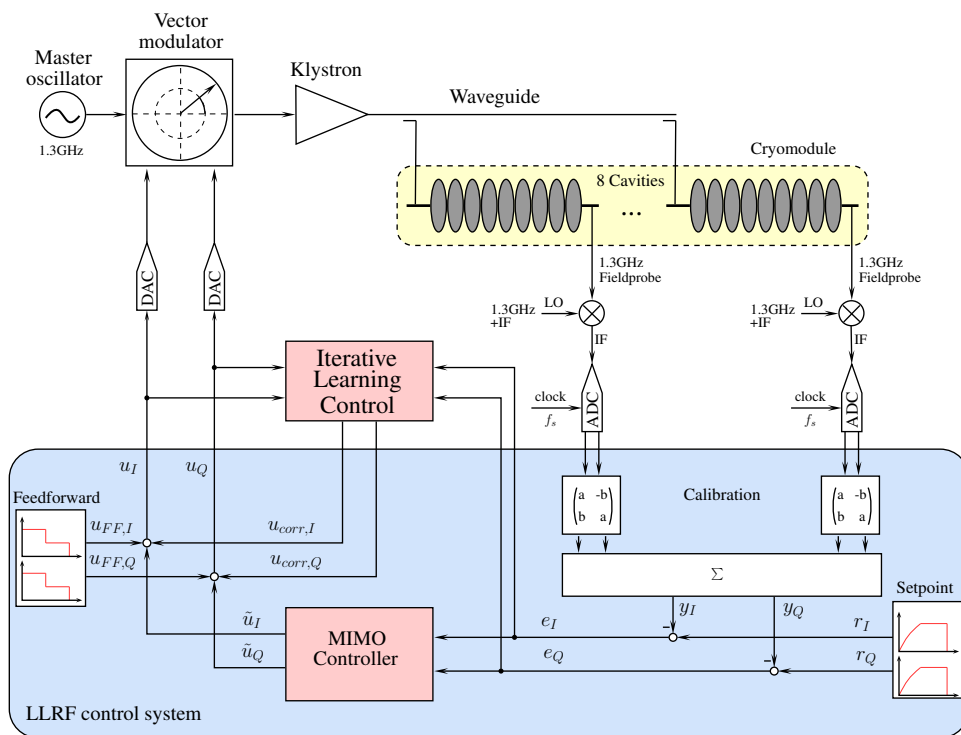


Fig. 46: LLRF system overview with plant and LLRF control system

5.1 RF field feedback loop

This example is performed at the FLASH based on the description in Ref. [17]. FLASH is operated in a pulsed mode with 10 Hz repetition rate and a pulse length of about 1 ms, see Fig. 45.

Each RF pulse can be divided into three parts: the filling; the flattop, where the electron bunches are accelerated; and the decay. The regulation goal is to achieve a stability of $\Delta A/A \leq 0.01\%$ and $\Delta\varphi \leq 0.01^\circ$. Two main concepts are used; on the one hand, adaptation by learning from pulse to pulse, i.e., the optimization of the drive signal at 10 Hz, and, on the other hand, the feedback controller acting within an RF pulse, i.e., at 9 MHz sampling frequency. The system is controlled in the in-phase (I) and quadrature (Q) plane. Hence, the signals for regulation are mapped from the amplitude and phase representation. With this, the system has two inputs and two outputs, i.e., it is a MIMO system (Fig. 46).

The feedback controller is designed using H_∞ -norm optimization. To do this, a system model is required. This is created by adding, in addition to the nominal drive signal (the input to the system u),

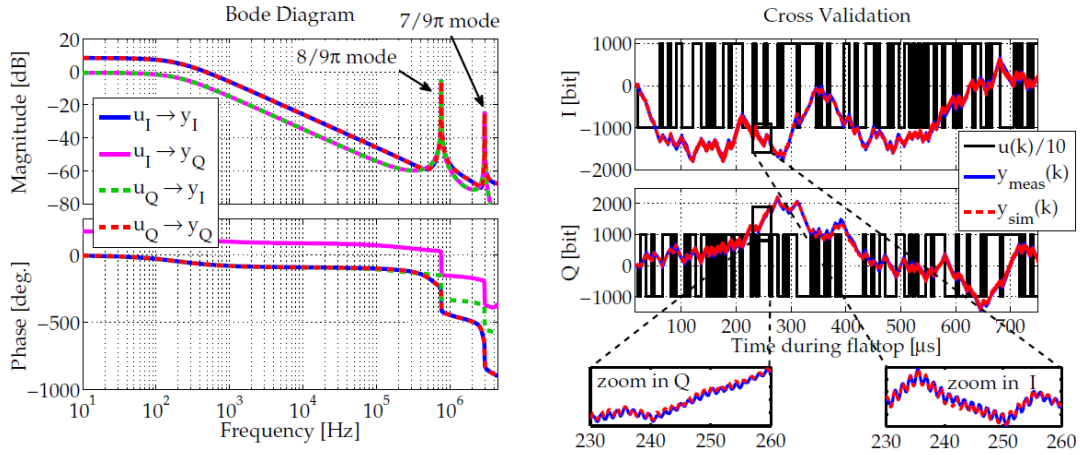


Fig. 47: Bode diagram of model and cross-validation, confirming system modelling

a small excitation signal. The change in output and its corresponding input signal are used to estimate a small signal model around the nominal operating point. In this way, the transfer matrix is estimated; its transfer functions (four in total for a 2×2 MIMO system) are given as a Bode diagram in Fig. 47. Furthermore, a cross-validation (the new excitation signal differs from the signal used for the system identification) shows the accuracy of the system identification.

With this model, the optimal MIMO controller coefficients based on an H_∞ approach are computed and follow the introduction in Section 4.5. Here, the weighting filters for closed-loop shaping are used to define the resulting closed-loop behaviour. The filter function for the controller sensitivity $W_{CS}(s)$ is chosen such that the controller must suppress the $7\pi/9$ resonance mode at 3 MHz; a notch filter at the analogue-to-digital converter for the $8\pi/9$ resonance mode is set such that this mode is not present in the error signal. The optimization is performed and leads to a MIMO controller with the control objectives of plant decoupling (no coupling from channel I to Q and vice versa), avoidance of passband mode excitation, and optimal closed-loop behaviour.

The idea of iterative learning control [21] for pulse-to-pulse feedforward adaptation is described in Ref. [22]. It is similar to the MIMO controller design for a model-based regulation scheme. The time-dependence within an RF pulse is given by $t = 0, \dots, T$, and the indices k and $k + 1$ represent the previous and current RF pulses, respectively. Given is a discrete linear time-invariant state space model,

$$\begin{aligned} x(t+1) &= Ax(t) + Bu(t), & x(0) &= x_0, & 0 \leq t \leq T, \\ y(t) &= Cx(t), \end{aligned}$$

of the closed-loop system $G(z)$, with the discrete time shift operator z . Mapping from continuous ($G_c = G(s)$) to discrete time ($G_d = G(z)$) can be done in MATLAB, using the command `Gd = c2d(Gc, Ts, 'tustin')`; T_s is the sampling time in seconds and 'tustin' the bilinear discretization method. Here, the closed-loop transfer function is given with the error as input ($u(t) \rightarrow e(t)$) and the controller output as output ($y(t) \rightarrow u(t)$), since the LLRF system is operating with MIMO feedback and the iterative learning control is acting on $u(t)$ with the signal to be minimized from pulse to pulse $e(t)$, see Fig. 41. The iterative learning control performance index is given by

$$J_{k+1}(u_{k+1}) = \frac{1}{2} \left(\sum_{t=1}^T e_{k+1}(t)^T Q(t) e_{k+1}(t) + \sum_{t=0}^{T-1} (u_{k+1}(t) - u_k(t))^T R(t) (u_{k+1}(t) - u_k(t)) \right),$$

where the weighting matrices $Q(t)$ and $R(t)$ are of compatible dimensions. This is the familiar performance criterion from linear quadratic optimal control theory. The optimal correction signal for the next RF

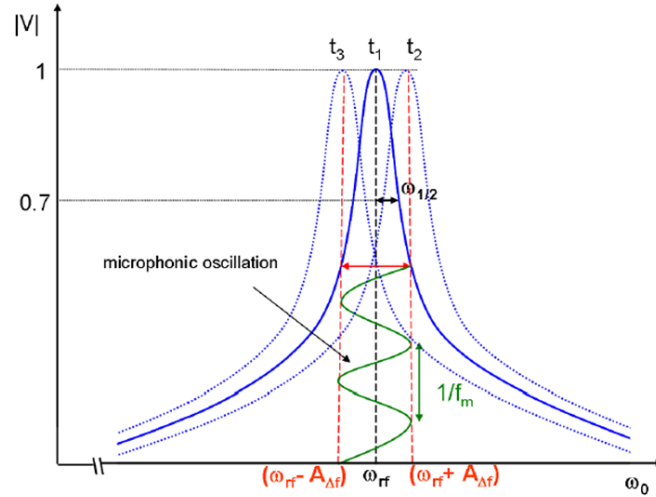


Fig. 48: Resonance frequency change by microphonics (courtesy: C. Schmidt)

pulse $u_{k+1}(t)$ is computed by

$$\begin{aligned}\xi_{k+1}(t) &= \beta(t)\xi_{k+1}(t+1) + \gamma(t)e_k(t+1), \\ u_{k+1}(t) &= u_k(t) + \omega\xi_{k+1}(t),\end{aligned}$$

where the required matrices $\beta(t)$, $\gamma(t)$, $\lambda(t)$, and ω are calculated by solving a Riccati equation backwards with the corresponding closed-loop model. For further information see, e.g., Refs. [17, 21, 22].

Using both feedback schemes, the MIMO controller, together with iterative learning control, the regulation goal in amplitude and phase stability are met and typically below the specification, i.e., $\Delta A/A \approx 0.008\%$ and $\Delta\varphi \approx 0.008^\circ$.

5.2 Microphonics suppression

Microphonics is one of the main disturbances acting to a cavity leading to small deformations of the cavity body. Such small deformations lead to an amplitude and phase error of a driven cavity caused by a detuning of the cavity from its resonance frequency, see Fig. 48.

The effect is mainly dominant for high Q_L ($Q_L > 10^7$) cavities used in continuous wave operation. However, even at FLASH, microphonics was observed during the construction of the European XFEL. FLASH is typically operated with $Q_L = 3 \times 10^6$, where microphonics is not the main disturbance source. This changes, by using e.g., a compacting machine at the XFEL injector (distance to FLASH is approx. 400 m) and its strong ground shaking, see Fig. 49. Here, the system performance gets worse (up to a factor of four during the work). Hence, a decoupling from the ground or all external noise sources is often the first approach. This could be confirmed for a continuous wave driven cavity by placing an anti-vibration mat below a vacuum pump, see Fig. 50. Such *passive noise reduction* helps improve the system performance. However, not all disturbance and noise sources can be avoided.

An *active microphonics reduction* for high Q_L ($Q_L > 10^7$) superconducting RF cavities was studied [23]. In this thesis, the main disturbances acting on a superconducting RF cavity were studied, see Fig. 51.

Furthermore, a system model is estimated, which consists of different mechanical cavity modes:

$$\begin{aligned}\Delta\ddot{\omega}_{\text{cav},k}(t) + 2\xi_k\omega_{m,k} \cdot \Delta\dot{\omega}_{\text{cav},k}(t) + \omega_{m,k}^2 \cdot \Delta\omega_{\text{cav},k}(t) &= \pm k_{\text{LF},k} 2\pi\omega_{m,k}^2 V_{\text{Piezo}}(t), \\ \Delta\omega_{\text{cav}}(t) &= \sum_k \Delta\omega_{\text{cav},k}(t),\end{aligned}$$

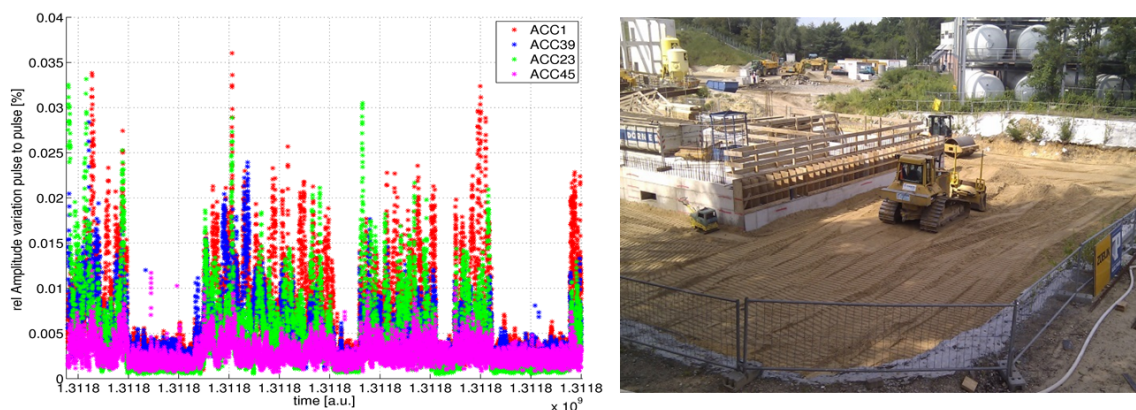


Fig. 49: Left-hand side, amplitude stability at the FLASH superconducting RF modules; right-hand side, compacting machine at XFEL injector (noise source).

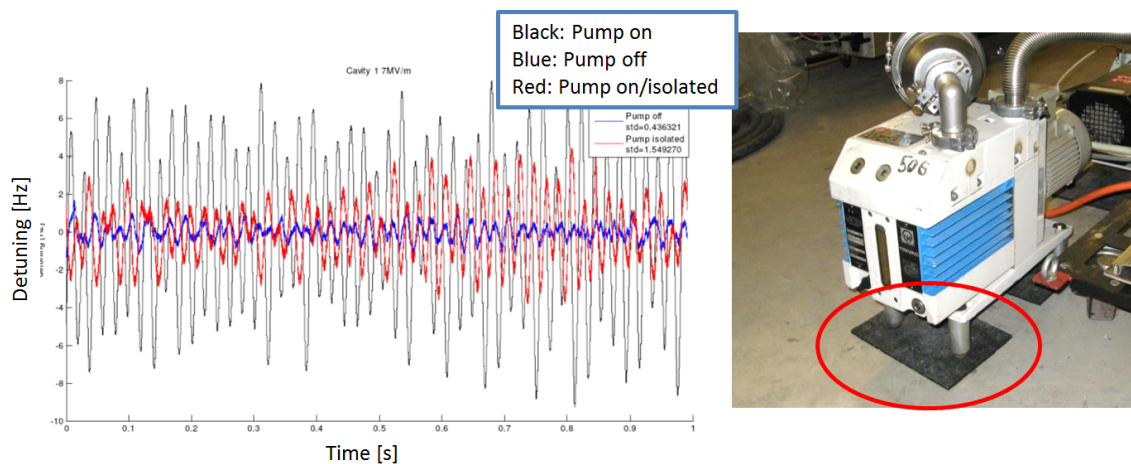


Fig. 50: Left-hand side, superconducting RF cavity detuning (courtesy: R. Rybaniec); right-hand side, vacuum pump as noise source (courtesy: J. Eschke).

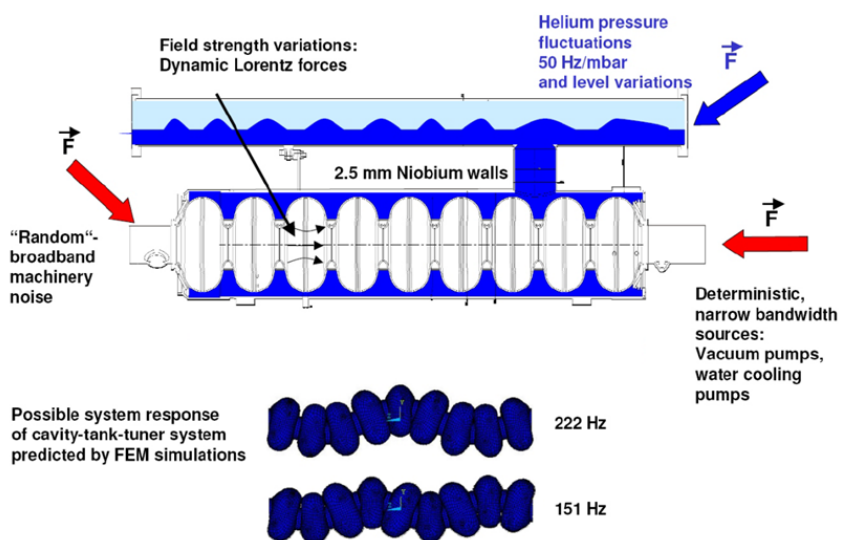


Fig. 51: TESLA cavity welded in cryo-unit; possible detuning sources are depicted [23]

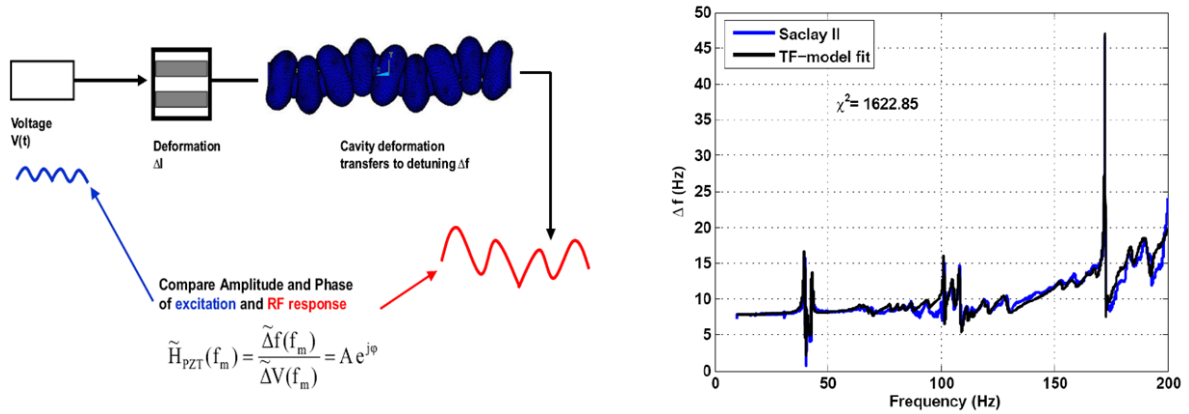


Fig. 52: Left-hand side, principle of transfer function measurement; right-hand side, model transfer function in frequency range of 10–200 Hz [23].

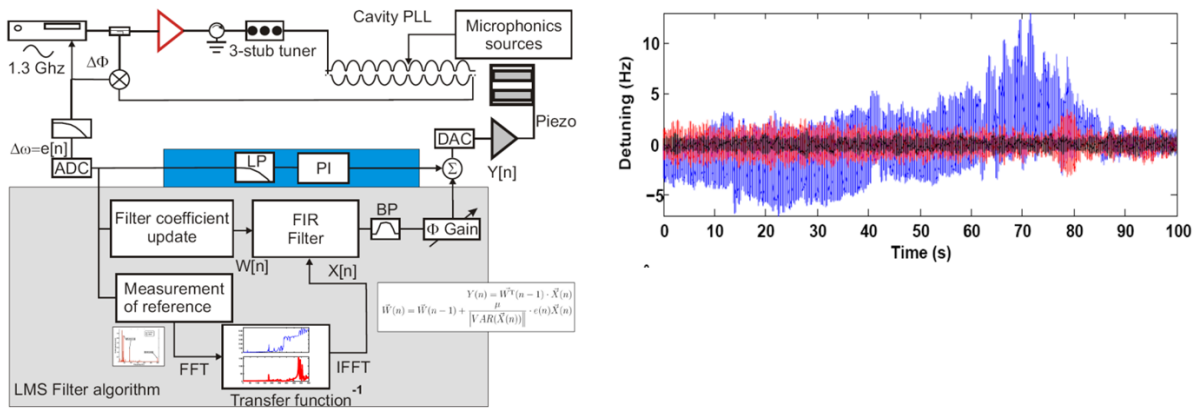


Fig. 53: Left-hand side: detuning compensation scheme given by a feedback and an adaptive feedforward signal path. Right-hand side: time-domain detuning data in open loop (blue), PI controller (red), and combined feedback and feedforward control (black).

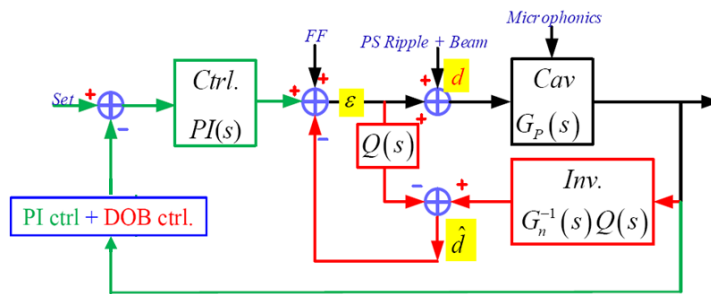


Fig. 54: Disturbance observer-based control scheme in combination with PI feedback loop [26]

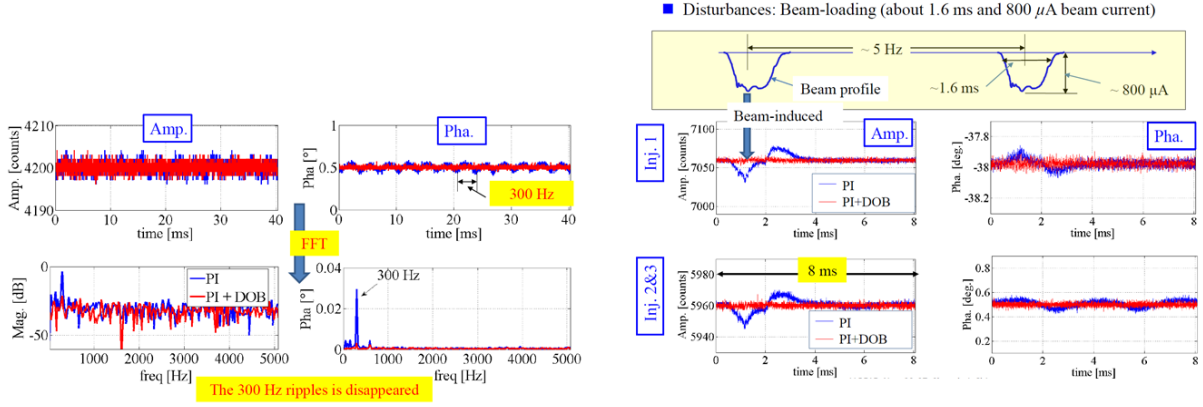


Fig. 55: Left-hand side, power supply ripple reduction using disturbance observer-based control; right-hand side, beam-induced disturbance rejection [26].

with the applied piezo voltage V_{piezo} as input and the corresponding eigenmode detuning $\Delta\omega_{\text{cav},k}$ as output. Thus, the model for each mode k in frequency domain using Laplace transform is given as

$$H_k(s) = \frac{\omega_k^2 M_k}{s^2 + 2\xi_k \omega_k s + \omega_k^2}.$$

Together with a low-pass behaviour and a time delay, the total system model is

$$H(s) = \left(H_0(s) + \sum_{k=1}^N H_k(s) \right) \cdot H_{\text{delay}}(s),$$

with

$$H_0(s) = \frac{M_0}{\tau s + 1} \text{ (low-pass)}$$

and

$$H_{\text{delay}}(s) = \exp(-T_{\text{delay}} \cdot s) \text{ (time delay)}.$$

A model is identified for the Saclay II tuner and its measured and estimated transfer function is shown in Fig. 52. Based on this model a controller consisting of a feedforward and feedback scheme is designed, as shown in the left panel of Fig. 53. The resulting detuning stability for a superconducting RF cavity operated at 1.8 K with $Q_L = 6.4 \times 10^7$ is shown on the right panel of Fig. 53. For further information, see Refs. [23] and [24].

5.3 Disturbance rejection

Reference [25] describes the application using a disturbance observer-based control scheme for LLRF systems. It is in use at the compact energy recovery linac at KEK. In the following, a brief outline of this topic is given. Assume, a disturbance acting on the system, and that, for this example, the disturbance is not precisely measurable. However, a disturbance observer can be used to estimate the disturbance. This requires a sufficiently precise system model $G_P(s)$. The system output is filtered by the inverse system transfer function $G_n^{-1}(s)$ together with a filter function $Q(s)$, see Fig. 54. This filter function is needed to low-pass filter high-frequency components, to set the frequency region of interest for the expected occurring disturbance and to cope with the inversion of causal systems. Furthermore, it is necessary to

filter the system input (known from the drive signal) by the same filter function. The difference between the filtered drive signal and the estimated drive signal computed from the output signal is an estimate of the disturbance. This estimated disturbance signal is subtracted from the drive, i.e., in the best case, the subtracted estimated disturbance and the real disturbance cancel.

Beside this feedforward disturbance cancellation, a PI feedback loop is added as an outer loop. This further reduces the occurrence of disturbances that are not compensated by the disturbance observer-based control scheme. Two examples are given in Fig. 55: the suppression of power supply ripples and the beam-induced voltage decrease. Both examples show that using advanced control schemes helps to improve the system performance. For further details, see Ref. [25].

Acknowledgements

I warmly thank J. Branlard, M. Hoffmann, G. Lichtenberg, H. Schlarb, and C. Schmidt for their support and helpful comments during the preparation of this lecture and for proofreading this contribution. I wish to acknowledge in particular, for the material provided: J. Eschke, M. Hoffmann, T. Miura, A. Neumann, M. Omet, F. Qiu, R. Rybaniec, T. Schilcher, and C. Schmidt.

References

- [1] W. Anders *et al.*, Status report of the Berlin Energy Recovery Linac Project bERLinPro, in IPAC2016, Busan, Korea, 2016, p. 1827.
- [2] P. Echevarria *et al.*, First LLRF tests of bERLinPro gun cavity prototype, in IPAC 2016, Busan, Korea, 2016, p. 1831.
- [3] *bERLinPro—SC RF Accelerating Structures*, 2016. https://www.helmholtz-berlin.de/projects/berlinpro/bpro-groups/srf_en.html
- [4] N. Nakamura *et al.*, Present status of the compact ERL at KEK, in Proc. 5th International Particle Accelerator Conf. (IPAC 2014): Dresden, Germany, 2014, p. MOPRO110. <http://jacow.org/IPAC2014/papers/mopro110.pdf>
- [5] T. Miura *et al.*, Low-level RF system for cERL, IPAC 2010, Kyoto, Japan, 2010, p. 1440.
- [6] *IMS—Image Archive*, 2016. <https://www2.kek.jp/imss/eng/library/>
- [7] *Free-Electron Laser FLASH*, 2016. <http://flash.desy.de/>
- [8] S. Di Mitri, Bunch length compressors, *CAS: FELs and ERLs*, Hamburg, Germany, 2016.
- [9] M. Hoffmann, Ph.D. thesis, Hamburg-Harburg University of Technology, 2008. <http://www-library.desy.de/cgi-bin/showprep.pl?desy-thesis-08-028>
- [10] Z. Geng and S. Simrock, Evaluation of fast ADCs for direct sampling RF field detection for the European XFEL and ILC, *LINAC*, Victoria, BC, Canada, 2008, p. 1030.
- [11] T. Schilcher, Ph.D. thesis, Hamburg University, 1998.
- [12] M. Omet *et al.*, Development and test of klystron linearization packages for FPGA-based low level RF control systems of ILC-like electron accelerators, 2014 19th IEEE-NPSS Real Time Conf. (RT), 260030, 2014 (IEEE, Piscataway, NJ, 2014), p. 1.
- [13] *9-cell TESLA-Type SRF-Cavity*, 2016. http://tt.desy.de/desy_technologies/accelerators_magnets_und_cryogenic_technologies/weld_free_cavity/index_eng.html
- [14] E. Vogel, *Phys. Rev. Spec. Top. Accel. Beams* **10** (2007) 052001.
- [15] *Laplace Transform*, 2016. https://en.wikipedia.org/wiki/Laplace_transform
- [16] L. Ljung, *System Identification, Theory for the User*, 2nd ed. (Prentice-Hall, Upper Saddle River, NJ, 1999).
- [17] S. Pfeiffer, Ph.D. thesis, Hamburg-Harburg University of Technology, 2014. <https://doi.org/10.15480/882.1191>

- [18] S. Skogestad and I. Postlethwaite, *Multivariable Feedback Control: Analysis and Design*, 2nd ed. (Wiley, Chichester, 2005).
- [19] R.G. Lyons, *Understanding Digital Signal Processing*, 2nd ed. (Prentice Hall, Upper Saddle River, NJ, 2004).
- [20] G. Stein, *IEEE Control Syst.*, **23** (2003) 12. <http://dx.doi.org/10.1109/mcs.2003.1213600>
- [21] N. Amann *et al.*, *IEE Proc. Control Theory Appl.* **143** (1996) 217.
- [22] C. Schmidt, Ph.D. thesis, Hamburg University of Technology, 2010. <http://www-library.desy.de/cgi-bin/showprep.pl?desy-thesis-11-019>
- [23] A. Neumann, Ph.D. thesis, Humboldt University of Berlin, 2008. <http://edoc.hu-berlin.de/docviews/abstract.php?id=29419>
- [24] A. Neumann *et al.*, *Phys. Rev. Spec. Top. Accel. Beams* **13** (2010) 082001. <http://link.aps.org/doi/10.1103/PhysRevSTAB.13.082001>
- [25] F. Qiu *et al.*, *Phys. Rev. Spec. Top. Accel. Beams* **18** (2015) 092801. <http://link.aps.org/doi/10.1103/PhysRevSTAB.18.092801>
- [26] F. Qiu, Disturbance observer-based control in low-level radio-frequency system in a compact energy recovery linac at KEK, in *LLRF Workshop 2015*, Shanghai, China, 2015.